ELI Gammatron Beamline: A Dawn of Ultrafast Hard X-ray Science

U. Chaulagain [1,*], M. Lamač [1,2], M. Raclavský [1,3], K. P. Khakurel [1], Kavya H. Rao [1], K. Ta-Phuoc [4], S. V. Bulanov [1,5] and J. Nejdl [1,3]

1   ELI Beamlines Centre, FZU-Institute of Physics of the CAS, 252 41 Dolní Břežany, Czech Republic
2   Faculty of Mathematics and Physics, Charles University, Ke Karlovu 3, 121 16 Prague, Czech Republic
3   Faculty of Nuclear Sciences and Physical Engineering, Czech Technical University, Břehová 78/7, 115 19 Prague, Czech Republic
4   Laboratoire d'Optique Appliquée, Ecole Polytechnique, ENSTA, CNRS, Institut Polytechnique de Paris, 91120 Palaiseau, France
5   National Institutes for Quantum and Radiological Science and Technology (QST), Kansai Photon Science Institute, 8-1-7 Umemidai, Kizugawa 619-0215, Kyoto, Japan
*   Correspondence: uddhab.chaulagain@eli-beams.eu

Abstract: The realization of compact X-ray sources is one of the most intriguing applications of laser-plasma based electron acceleration. These sources based on the oscillation of short micron-sized bunches of relativistic electrons provide femtosecond X-ray pulses that are collimated, bright, and partially coherent. The state-of-the-art laser plasma X-ray sources can provide photon flux of over 10^{11} photons/shot. The photon flux can further be enhanced with the availability of high repetition rate, high-power lasers, providing capacities complementary to the large scale facilities such as synchrotrons and X-ray free-electron lasers. Even though the optimization of such sources has been underway for the last two decades, their applications in material and biological sciences are still emerging, which entail the necessity of a user-oriented X-ray beamlines. Based on this concept, a high-power-laser-based user-oriented X-ray source is being developed at ELI Beamlines. This article reports on the ELI Gammatron beamline and presents an overview of the research accessible with the ultrashort hard X-ray pulses at the ELI Gammatron beamline.

Keywords: laser wakefield acceleration; betatron radiation; inverse compton radiation; phase-contrast imaging; warm dense matter; laser plasma interaction; X-ray absorption spectroscopy; X-ray diffraction; X-ray emission spectroscopy

1. Introduction

Since their discovery more than a century ago, X-ray-based diagnostics have extended our fundamental understanding of matter and are being used in countless fields of research and practice, including medical diagnostics, fundamental research (in physics, chemistry, and biology), materials science, and engineering [1–4]. Short wavelengths allow atomic-scale probing of the structure of matter, and their weak interaction with inner-shell electrons ensures deep penetration, enabling volumetric probing of dense objects. Even though conventional X-ray sources such as X-ray tubes and synchrotrons provide access to spatial resolution for molecular structure and the electron orbitals, they are unable to provide temporal resolution for the atomic and molecular motion on their natural time scale. New-generation facilities, such as the third-generation synchrotrons and X-ray free-electron lasers (XFELs), providing extremely bright, ultrashort X-ray sources (with a duration of few femtoseconds (fs)), play an important role here, as they support the investigation of ultrafast structural dynamics associated with phase transitions in condensed matter, rapid biological processes, and chemical reactions [5,6]. However, the number of and access to such facilities are rather limited. In this context, laser-based pulsed X-ray sources, both

coherent and incoherent, with unprecedented pulse durations down to attoseconds, are of utmost importance [7,8]. The highly coherent, short wavelength sources with short pulse durations (several tens of attoseconds) [8,9], based on high-order harmonic generation (HHG), which are available in many laser facilities, are limited to the extreme ultraviolet (EUV/XUV) or soft X-ray spectral range [10–12]. Sources based on laser wakefield acceleration (LWFA) [13] overcome this limitation by their ability to produce X-rays and γ-rays. Advancement in femtosecond high-power laser technology facilitates the generation of high-charge relativistic electron beams with energies ranging from a few megaelectron volts to more than 1 GeV within a few centimeters [14,15] via LWFA. These relativistic electrons offer the possibility of expanding the next generation of laser-driven X-ray sources. The plasma-based Betatron [16,17], which is one among them, employs relativistic electrons undergoing transverse oscillations within the accelerating process and generates partially coherent X-rays with a femtosecond pulse duration, a small source size, and a broad spectrum spanning from a few keV up to hundreds of keV [18].

When a relativistic electron bunch collides with an intense laser, the electrons oscillate in the field of the laser pulse and backscatter the radiation in the direction of the electron bunch via Thomson back-scattering (TS) or inverse Compton scattering (ICS), depending on the strength of the colliding laser pulse and the kinetic energy of the electrons. This interaction causes a double Doppler upshift in the frequency of the backscattered radiation, producing an intense γ-ray burst with photon energies that can reach the MeV range with current TW-class lasers [19,20]. Advances in laser and target technologies favor enormous improvements in the electron and X-ray beam quality [21,22] of both Betatron and ICS X-ray sources, which represent the next generation of compact hard X-ray sources. Recent experimental results on Betatron using laser systems with a few hundred terawatts of power revealed the ability to deliver beyond 10^{11} X-ray photons per pulse, which can further be increased by using PW-class lasers [23]. Properties such as pulse duration, operational wavelength, photon flux, brightness, and jitter-free synchronization between the driving laser and the generated X-rays provide a novel platform to study the ultrafast dynamics of matter.

The ELI-Beamlines Centre, located in the Czech Republic, is one of the pillars of the ELI (Extreme Light Infrastructure) project and is expected to be one of the most powerful laser facilities in the world [24,25]. One of the main goals within the ELI project is to provide ultra-short beams of particles and X-rays to a broad international user community for both fundamental and applied research in various fields. In addition, ELI Beamlines promotes novel laser-plasma accelerator techniques to deliver ultrashort particle and radiation sources with unique capabilities, which could strongly impact various scientific, industrial, and societal applications. With these remarkable capabilities, various multidisciplinary, user-oriented experiments are being implemented at ELI Beamlines [10,26–28].

Here, we report on the ELI Gammatron beamline, which is a multidisciplinary, user-oriented platform employing hard X-ray radiation based on LWFA. The Gammatron beamline will provide ultrashort, energy-tunable, collimated hard X-ray radiation with over 10^{11} photons per pulse for a broad range of user experiments. The beamline will provide ultrafast sources of broadband X-ray pulses ranging from a few kiloelectron volts to a few hundred kiloelectron volts in the Betatron scheme and narrow (~10–20% energy spread) or broadband pulses of hard X-rays in the spectral range of a few hundred keV to few megaelectron volts in the TS or ICS scheme. The Betatron, TS, and/or ICS schemes are realized mainly using the PW-class Ti:sapphire HAPLS laser L3 (30 J, 30 fs, 810 nm, 10 Hz), and the high-repetition rate DUHA laser L2 (5 J, 20 fs, 50 Hz), housed at ELI beamlines. Figure 1a compares the peak brightness (simulated) of laser-driven X-ray sources at ELI Beamlines to other available X-ray sources in the respective spectral range and Figure 1b shows the peak brightness of LWFA-based Betatron sources at different laser facilities. A dedicated user station was also designed to accommodate various time-resolved experiments.
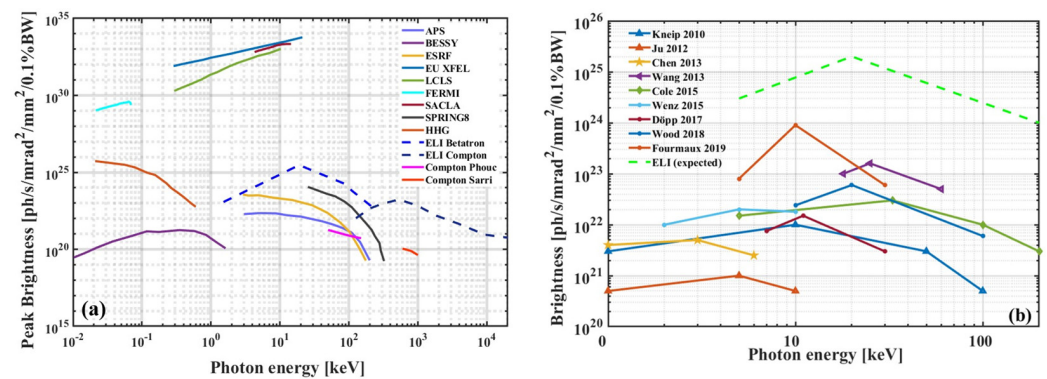
Figure 1. (**a**) Peak brightness for different X-ray sources: The APS synchrotron in the USA, the BESSY facility in Germany, ESRF in France, EU XFEL in Germany, the LCLS facility in the USA, FERMI in Italy, SACLA in Japan, the SPRING synchrotron facility in Japan, the HHG beamline at ELI Beamlines [10], the ELI Beamlines Gammatron beamline and all-optical Compton sources [19,29]. (**b**) Peak brightness of the laser plasma accelerator (LPA)-driven Betatron X-ray source at different laser facilities [30–38] and the expected brightness of the Betatron X-ray source at ELI Beamlines.

The article is organized as follows: Section 2 describes the mechanism of X-ray generation based on numerical simulations of LWFA, followed by the detailed design of the Gammatron beamline and associated diagnostics in Section 3, and various applications of the Gammatron beamline in Section 4.

2. Numerical Simulation of X/γ-ray Generation in the Gammatron Beamline

LWFA is one of the most promising methods for compact electron acceleration. In LWFA, electric fields of more than 100 GV/m [13] allow GeV kinetic energy gain in a centimeter-scale laser-produced plasma, which is unparalleled by the contemporary radio-frequency accelerators [39]. Electron acceleration at energies up to ~8 GeV in a decimeter-long plasma has been recently demonstrated in [15]. Furthermore, electrons injected off axis or with nonzero transverse momentum undergo an oscillatory motion throughout the acceleration and emit X-ray radiation.

Results of 3D PIC simulations of Betatron X-ray generation from LWFA electrons using the L3 HAPLS laser in the Gammatron beamline are presented here. The following parameters were considered in the calculation for a linearly polarized laser pulse: pulse duration (τ_{FWHM}) = 30 fs, focal spot diameter (d_{FWHM}) = 15.8 μm, wavelength (λ_0) = 808 nm, normalized vector potential (a_0) = 7.3, which corresponds to a laser pulse with the energy of 10 J and peak intensity $I_0 = 1.1 \times 10^{20}$ W/cm^2, for a fully ionized, pure He gas target with a length of 5 mm and plateau electron plasma density $n_e = 5 \times 10^{18}$ cm^{-3}. The evolution of energy distribution inside the target and the energy distribution after the acceleration process and electrons exit the gas target are given in Figure 2a,b, respectively. Due to the strong self-injection [40,41] from the laser field driving the LWFA process, an accelerated electron bunch with a total charge of 7 nC is produced, corresponding to 4.4×10^{10} electrons. The radiation emitted per unit frequency per solid angle was calculated according to the radiation integral [42] for electron trajectories obtained from the simulation and presented in Figure 3. Figure 3a shows the spatially integrated spectral distribution given in number of photons per 0.1% relative bandwidth. Synchrotron-like features with critical energy (E_c) = 11.4 keV and 4.2×10^9 photons/0.1% BW per shot emitted at critical energy, and the total photon flux of 8.6×10^{12} over the whole spectrum, are observed. Figure 3b shows the beam profile of the X-ray radiation with an angular divergence of ≈30 mrad FWHM. As the X-ray pulse duration copies the temporal profile of the relativistic electron bunch, a pulse duration of ~10 fs (FWHM) is expected. The Betatron X-ray photon brightness corresponding to these parameters is given in Figure 1.
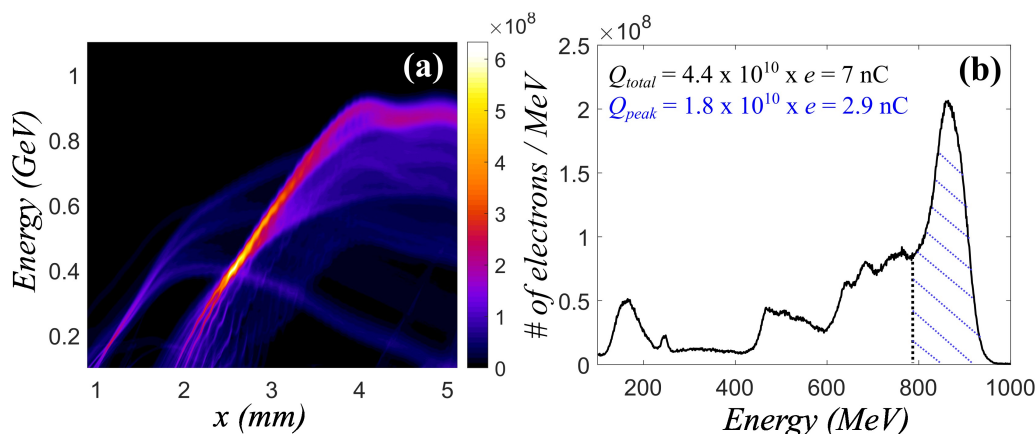
Figure 2. (**a**) Evolution of the electron spectrum inside the gas target. (**b**) Electron spectrum at the end of the gas target.
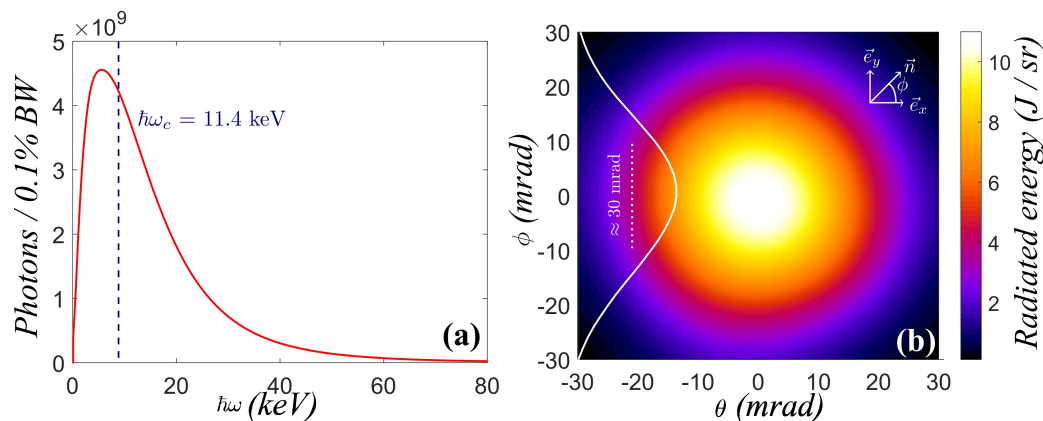

Figure 3. (**a**) The spectral distribution of Betatron photons per 0.1% bandwidth. (**b**) Angular distribution of radiated energy of the Betatron photons.

The recently proposed photon flux enhancement schemes can further enhance the usability of the Betatron X-ray source [43–46]. These results, and the micron-scale size of the radiating electrons, indicate the capacity of the Gammatron beamline to generate brilliant, femtosecond, broadband, collimated, and spatially coherent X-rays. The production of γ-rays can be accomplished by slightly modifying the Betatron X-ray's experimental setup, i.e, by introducing a thin, low-Z material foil downstream of the gas target, as demonstrated by Ta Phuoc et al. [17]. This foil, which is ionized by the leading edge of the incident laser pulse, acts as a plasma mirror and reflects the laser pulse towards the accelerating electrons, resulting in the ICS of the laser. A second laser pulse, split off from the L3 beam (L3 AUX), is available in the Gammatron beamline, which can be used as a scattering beam for ICS. This scheme offers better control of the source, allowing one to vary the laser intensity at the interaction site or the polarization of the laser. Figure 4 shows the results of such a laser–electron collision for $a_0 = 2$ and 500 MeV electron energy. With 10^{10} electrons, more than 10^6 ph/0.1% BW per shot at 10 MeV and 10^9 γ-photons per shot are estimated, along with divergence in the order of a few milliradians. The corresponding Compton X-ray brightness is shown in Figure 1, indicating that the Gammatron beamline will potentially be one of the most brilliant γ-ray sources in the world.
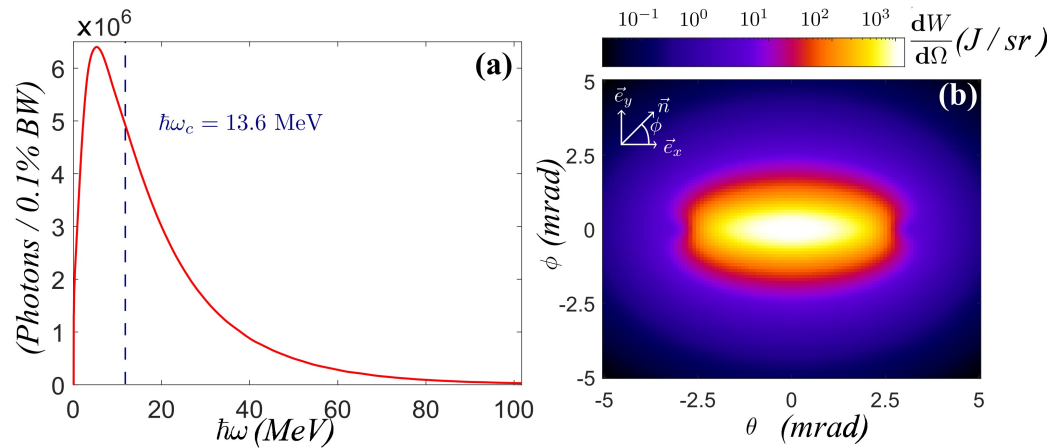
Figure 4. (**a**) The spectral distribution of photons per 0.1% bandwidth; (**b**) angular distribution of radiated energy in the ICS scheme.

3. High-Repetition-Rate Gammatron Beamline

The Gammatron beamline, located in experimental Hall E2 (Figure 5), will deliver femtosecond X-rays in a wide spectral range. In the Betatron scheme, the source will operate in a broadband energy regime (a few kiloelectron volts to a few hundred kiloelectron volts), and in the ICS scheme, the source will operate either in a broadband or in a quasi-monoenergetic regime (MeV regime), depending on the accelerated electrons and the intensity of the counter-propagating laser. As discussed in Section 2, for appropriate experimental parameters (laser intensity, spot size, pulse duration, and density profile of the gas target), electrons are accelerated to relativistic velocities by LWFA and wiggled by the plasma itself or by collision with another laser pulse, resulting in the emission of intense femtosecond X-ray or γ-ray beams. The characteristics of the radiation produced will depend on the requirement of the end-user.
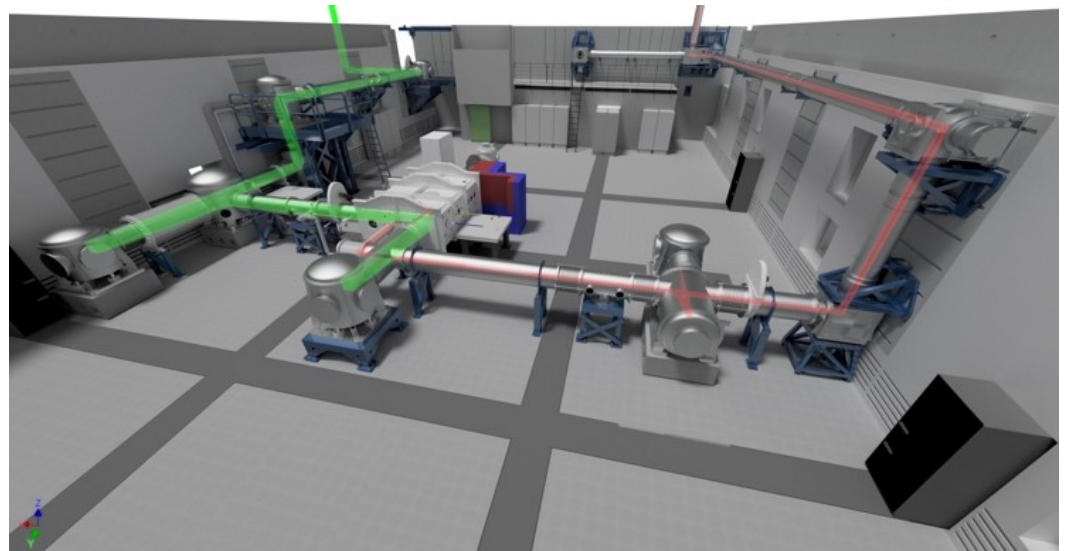
Figure 5. Rendering of the ELI Gammatron beamline located in experimental hall E2. The solid green beam is the PW-class HAPLS laser L3, and the solid red beam is the DUHA laser L2.

The Gammatron beamline will be driven by the two state-of-the-art lasers at ELI beamlines: the PW-class HAPLS laser L3, which is already operational, and the high-repetition rate DUHA laser L2 [47], which will be operational soon. In the first phase of the Gammatron beamline, the L3 laser with a 215 mm × 215 mm (super-Gaussian) beam and maximum pulse energy of 10 J will be used. The L3 beam propagates a distance of

49 m from the compressor to the Gammatron interaction chamber via seven high-damage-threshold multi-layer dielectric mirrors [48]. The beam transport is designed with very high vibration stability of all the structures supporting the transport mirrors and optomechanics sized $440 \times 290 \times 75$ mm for the turning mirrors. The vibration response is minimized by pushing the eigen frequencies of components above 75 Hz and by setting high stiffness for all supports, breadboards, and optical mounts [49]. A laser beam pointing stability of <1 mrad is expected.

3.1. Experimental Configurations

The Gammatron beamline will operate in two configurations: (1) the Betatron scheme, where only one laser will drive the LPA and generate X-ray pulses via Betatron radiation, and (2) the TS or ICS scheme, where two laser beams will be used.

In the TS/ICS scheme, one laser beam will drive the LPA, and the other, counter-propagating, will collide with the relativistic accelerated electrons at the exit of the LPA to generate X-rays or γ-rays. The experimental setup to realize the Betatron scheme, along with its various diagnostics, is shown in Figure 6.
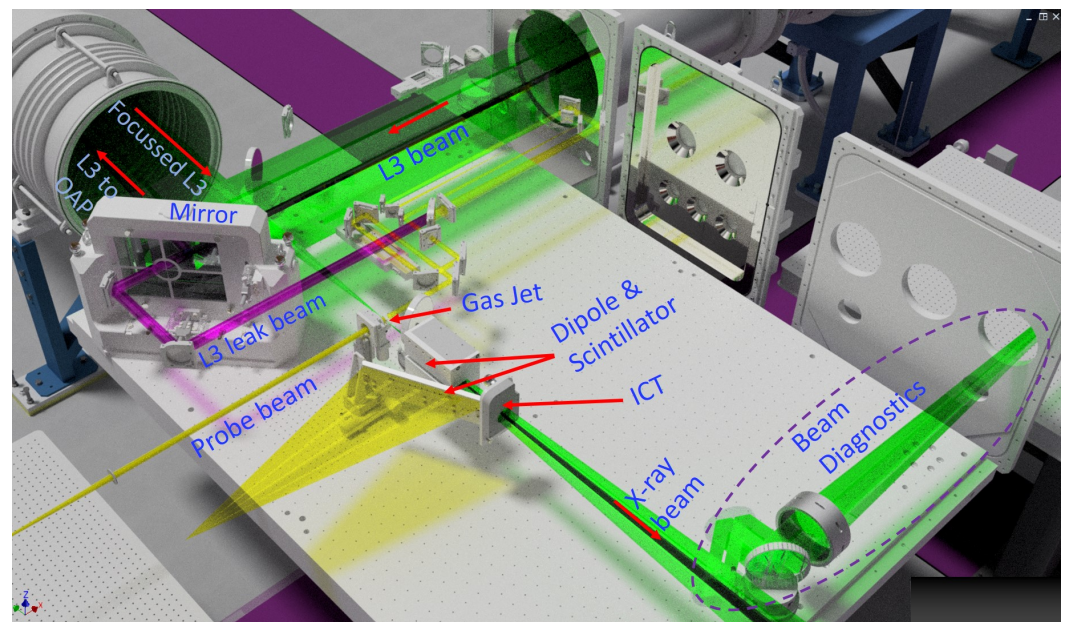

Figure 6. Detailed view of the Gammatron beamline operating in the Betatron scheme and the associated diagnostics inside the interaction chamber.

An off-axis parabolic mirror (OAP) with a focal length of 4000 mm (F-number of $\sim$19) focuses the L3 beam on a few cm long gas jet and drives LWFA, generating Betatron X-rays. The E2 hall is designed to handle the focusing optics up to an F-number of 50.

Figure 7 shows the ICS scheme, where the L3 beam focused on the gas jet or a cell by the OAP (same as in the Betatron scheme) accelerates the electrons to GeV energies via LPA, and a second high-power laser beam, split off either the L3 beam (L3 AUX) or the L2 beam, will be used to drive the ICS source. The second scattering laser beam (L3 AUX or L2) will be focused on the downstream portion of the gas jet using a short-focal-length OAP with a fixed off-axis angle of about $20°$ and an F-number of 1.5, providing a peak intensity of few times 10^{20} W/cm^2 at the focus, corresponding to $a_0 \sim 10$. In the absence of a second high-power scattering laser, the plasma mirror technique mentioned in [17] will be implemented by employing the L3 laser to accelerate electrons and generate X-rays in the ICS scheme. In addition, a low-power L3 AUX will be combined with the high-power L3 beam to generate an energy-tunable Thomson scattering source (TS) in a weak non-linear regime. The diagnostics for laser, plasma, and electrons will be the same for both schemes.
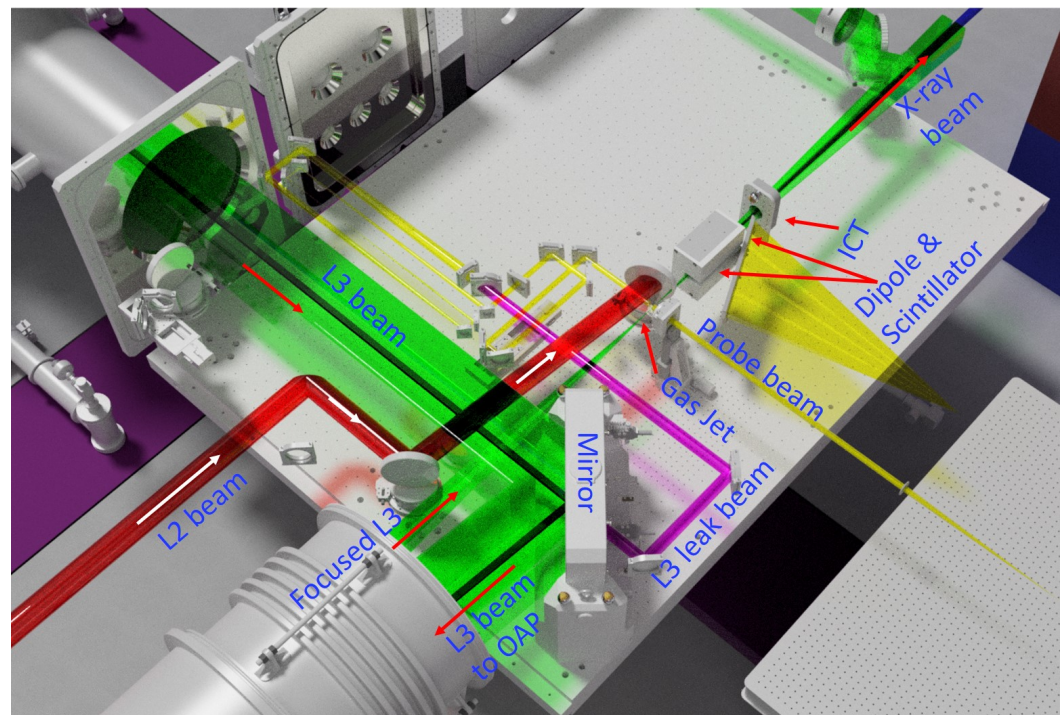
Figure 7. Detailed view of the Gammatron beamline operating in the ICS scheme and the associated diagnostics inside the interaction chamber. An L3 beam drives the LPA, and an auxiliary laser beam (split off of L3 or L2 (red)) will be used as a scattering beam which is focused on the downstream portion of the gas jet using a short-focal-length OAP.

3.2. Targetry

In LWFA experiments, gas targets with various density profiles are routinely used. The commonly used gases are He, N_2, an admixture of He with N_2, dry air, Ar, and gas clusters [34,50–52]. These gas jet targets routinely employ complex gas density distributions (e.g., tailored gas density [45], enabling the optimization of both the electron acceleration and the X-ray generation from the accelerated electron bunches. Targets with asymmetric density profiles, generated either by pulsed valves with nozzles of various shapes or by gas streams perturbed by obstructions such as razor blades or wires, provide better control of electron acceleration [53], increased charge, improved shot-to-shot stability, and/or less energy spread. Precise evaluation of the gas density profile is therefore critical for benchmarking numerical simulations with experimental results. A dedicated gas target characterization station that can measure the neutral gas density in both axially symmetric and asymmetric nozzles with very high resolution and sensitivity is installed in E2. The novel probing scheme utilizing multi-pass interferometric imaging [54,55] has demonstrated increased phase sensitivity and near diffraction-limited spatial resolution [56]. The configuration shown in Figure 8 employs two relay-imaging arms and polarization switching to facilitate four passes of the probe beam through the gas jet. This scheme was validated in [56] by the tomographic characterization of low-pressure He gas jets with tailored density distribution, which is a typical LWFA target.

3.3. Laser and Plasma Diagnostics

A set of diagnostic techniques designed to characterize the driving laser beam in the interaction area and the laser-matter interaction in the Gammatron beamline is briefly outlined here.

3.3.1. Laser Diagnostics

Controlling the wavefront of the laser beam and the correction of its abberations are crucial for efficient LWFA and for the stability of the electron and X-ray beam distribution.
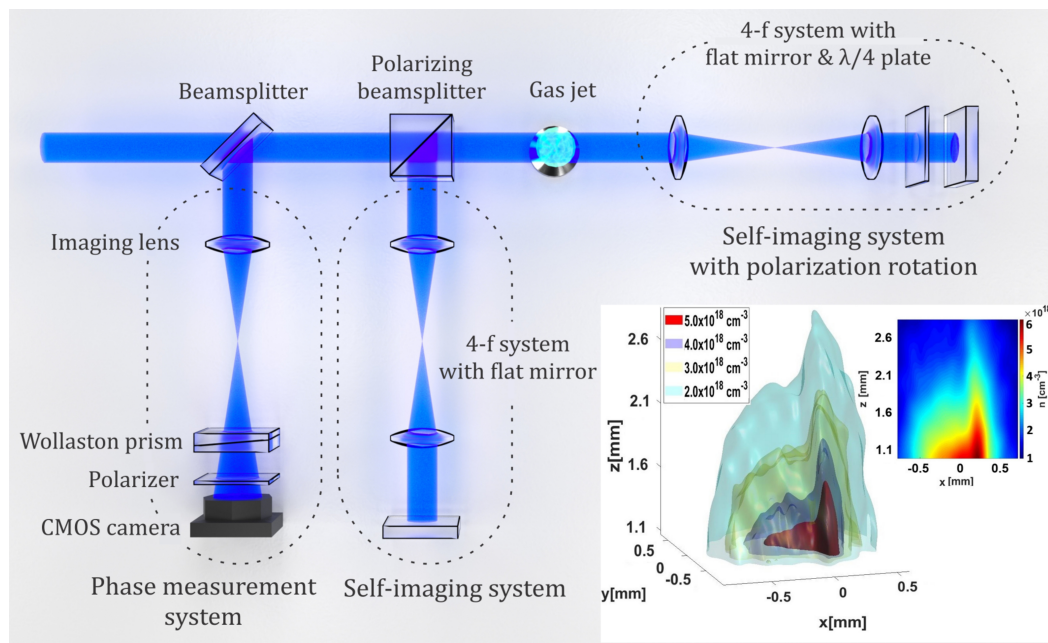
Figure 8. Schematic of the four-pass interferometric gas jet characterization. Tomograph of the density reconstruction of a helium gas jet (with a back-pressure of 7 bar) obstructed by a razor blade placed above the nozzle (inset), adapted from [56].

Wavefront distortions cause spatial inhomogenities in the midfield laser intensity distribution and drive an inhomogeneous transverse wakefield, which in turn adversely affects the electron beam distribution. In-vacuum and in-air diagnostics are developed to control both the near-field and far-field of the laser pulse. An in-vacuum wave-front-sensor (WFS), along with the focus diagnostics, using a high-quality microscope objective, will be implemented to characterize the laser focus at a reduced laser power level. The in-air diagnostics, placed outside the vacuum chamber, provide simpler access to both the near-field and the far-field measurements of the laser beam at full power. In addition, a closed-loop deformable mirror (DM) system located close to the interaction chamber will be used to correct the wavefront aberrations and control the interaction of the laser pulse with the target. The WFS placed beyond the focus allows the DM to reduce the aberrations due to all optical elements, including the focusing optics.

3.3.2. Laser–Plasma Interaction Diagnostics

A beam split off the driving beam (Figure 7) will be used to probe the interaction area and obtain information on laser propagation inside the gas target. In situ shadowgraphy and interferometry will be used to characterize the interaction of the laser pulse with the gas and to measure the electron density of the plasma in every shot. Information on both spatial distribution and the temporal evolution of the plasma can be retrieved by varying the probe delay with respect to the LPA driving beam. In addition, a TS-based diagnostic relying on the laser light scattering by the plasma electrons oscillating in the laser field will also be implemented to provide information on the propagation the laser beams inside the gas target. These diagnostics will be used to overlap the three laser beams, in time and space, for the ICS experiment.

3.4. Particle and Radiation Diagnostics

3.4.1. Electron Diagnostics

As discussed in previous sections, energies of the accelerated electrons in the Gammatron beamline will span from a few hundred megaelectron volts to a few gigaelectron volts. The electron bunch generated here will be characterized by their geometrical properties (emittance, divergence, and pointing stability), bunch charge, and energy spectrum, using

various diagnostics. The electron bunch profile and the pointing will be monitored using a scintillator screen imaged with a high-dynamic-range CCD camera. The parasitic light from the scintillator will be avoided by employing a bandpass filter at the scintillator emission wavelength. The energy spectrum of the generated electron beam will be characterized using a magnetic dipole electron spectrometer (ES), which is designed to have a modular configuration to accommodate the large range of electron energies with sufficient resolution. A 20 cm long ES module (comprising two 10 cm long magnet modules), shown in Figure 9a, is used in the Gammatron beamline for electron diagnostics. A total magnet length of up to 50 cm can be obtained by attaching 10 cm long dipole modules to attain the desired length. A series of Ce:YAG scintillation screens or Lanex screens are imaged with a high dynamic-range CCD camera. The images reveal the spectrum of the electron bunch. This detection system is also capable of providing electron-bunch charge measurements by calibrating the CCD camera, the imaging optics, and the scintillating screen [57]. In addition to the spectral measurement, a calibrated integrated current transformer (turbo ICT, Bergoz instrumentation) will be placed downstream of the electron path to measure the absolute charge of the electron bunches between 10 fC and 10 nC.

3.4.2. X-ray Diagnostics

Various types of X-ray diagnostics are designed to characterize the generated X-rays. First, the X-ray beam profile will be obtained by placing a X-ray camera (sensitive to energies <20 keV) or a scintillator screen (imaged with a high dynamic range CCD camera—for >20 keV). The following diagnostics will be used to measure the spectrum.

a. **Single-photon-counting X-ray CCD**: In the low-photon energy range (<20 keV), a single-photon counting method using a deep depletion X-ray CCD placed a few meters from the X-ray source will be employed. Filters placed in front of the detector will attenuate the X-ray signal, allowing the detection of less than one photon per ten pixels on average. The signal generated in one detection event is therefore directly proportional to the photon energy. An array of scintillators coupled with a position-sensitive photomultiplier tube can be used for a high energy range to enable the spectral measurement in single-photon counting mode.

b. **Ross filter Spectrometer**: In the hard X-ray range (<100 keV), spectrum measurement using the Ross filter pairs will be implemented. Each pair of Ross filters consists of two carefully selected filters of different materials and thicknesses that create closely matching transmittances differing only in their K absorption edges, which define their operational energy ranges. The difference in the signal detected by a CCD camera behind each filter of the pair is directly proportional to the number of photons in the chosen energy range. This method evaluates the spectrum up to 90 keV using 10 spectral bands, and the X-ray spectrum is reconstructed using the filter transmission values and by fitting the data with a selected function (e.g., the synchrotron radiation function). Figure 9b,c shows the ELI Beamlines high energy X-ray spectrometers based on the Ross filter technique. The high-energy spectrometer covers the X-ray spectrum from 8 to 88 keV and makes use of 18 different filters (listed in Table 1). Transmission measurements using thick filters will be implemented for X-rays > 100 keV.

c. **HAPG crystal spectrometer**: A crystal spectrometer with high spectral resolution and high sensitivity, based on diffraction from a highly annealed pyrolytic graphite (HAPG) mosaic crystal ($2d$ = 6.708 Å), will be implemented, in addition to the Ross-filter-based spectrometer mentioned above. The main features of the crystal spectrometer are its high spectral resolution and high sensitivity. The incoming X-ray photons are tightly focused on the CCD camera because of the cylindrical geometry of the crystal. Due to the low divergence of Betatron X-rays, a large number of emitted photons will be collected by the crystal and recorded on a narrow spectral line. The thickness and radius of curvature of the crystal were chosen to be 100 μm and 103.4 mm, respectively, to obtain the appropriate spectral resolution. Both the crystal and the CCD camera will be placed in long-travel-range linear stages, allowing

scanning of energy by varying the crystal's position with respect to the source. Measuring the X-ray signal at three different positions provides six data points with first- and second-order diffraction, providing an alternative and more accurate method to measure the Betatron spectrum. In addition, this spectrometer can also be employed in static X-ray absorption spectroscopy, as reported in reference [58].

Table 1. The ELI high-energy Ross-filter-based spectrometer and its filter combination to cover the 8–88 keV spectral range.

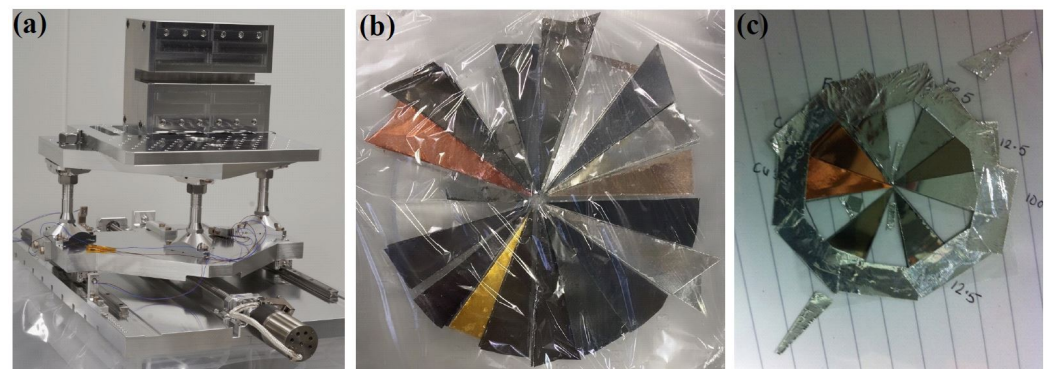| Filter Set	Foil Combination	Energy Band (keV)
1	Ge 50 µm/Cu 37.5 µm	8–11
2	Zr 45 µm/Ge 100 µm	11–18
3	Mo 50 µm/Zr 90 µm	18–20
4	Ag 72 µm/Mo 100 µm	20–25.6
5	Sn 93 µm/ Ag 72 µm	25.6–29.4
6	Nd 100 µm/Sn 150 µm	29.4–43.6
7	Dy 50 µm/Nd 75 µm	43.6–53.8
8	Ta 40 µm/Dy 100 µm	53.8–67.2
9	Au 55 µm/Ta 80 µm	67.2–80.5
10	Pb 85 µm/Au 55 µm	80.5–88.1

Figure 9. (**a**) A 20 cm long electron spectrometer with the dipole magnet on a motorized base. The ES has a 20 mm gap with a uniform magnetic field of about 1 T at the center of the gap. (**b**) The ELI high-energy Ross-filter-based spectrometer (spectral range: 8 keV to 88 keV) consisting of 10 filter pairs made of 18 metallic foils. (**c**) Ross-filter pairs employing 9 thin filters to cover the lower spectral energy range (3–20 keV).

3.5. X-ray Beam Transport and Focusing Optics

X-ray focusing optics are necessary for X-ray beam delivery at the user end-station, and several optical designs can be used according to the spot sizes requested. These designs include the use of a grazing-incidence toroidal mirror to refocus the beam, the use of mirror pair in a Kirkpatrick–Baez (KB) configuration, or the use of highly reflecting mosaic crystals. A dedicated multi-lane, multi-layer-coated X-ray optics instrument based on a KB configuration that is capable of focusing the X-ray beam in both horizontal and vertical directions was designed to serve as the versatile focusing optics for the Gammatron beamline [59]. The mirror system consists of three lanes coated with multiple layers, each lane being optimized for a specific spectral band spanning from 1 to 25 keV with high reflectivity. The mirror system was designed such that each reflective unit has a reflectance of over 60% at a grazing incidence angle of ~5 mrad.

3.6. Multidisciplinary User Station

A multidisciplinary Gammatron User Station (GaUS) was designed to cater to various experiments. The main part of GaUS consists of a vacuum chamber (1 m diameter) with a

30 mm thick decoupled aluminum breadboard, pumped by a turbomolecular pump with a pumping speed of over 2100 l/s. The GaUS chamber is connected to the interaction chamber by a DN200 aluminum tube, allowing the vacuum transport of both the X-ray pulse and the IR pulse. An auxiliary IR beam split from the main LPA driving beam and synchronized with the X-ray beam is provided at the user station to facilitate time-resolved pump-probe experiments. The IR pump beam is focused using an off-axis parabola with a hole, allowing collinear focusing. The X-ray focal spot is imaged using a Ce:YAG scintillator screen mounted on a motorized stage. The schematic of the interior of the GaUS station, along with the setup for simultaneous time-resolved X-ray spectroscopy and diffraction experiments, is given in Figure 10. The GaUS station is also equipped with the state-of-the-art instruments for sample mounting and detectors for scattered X-ray photons.
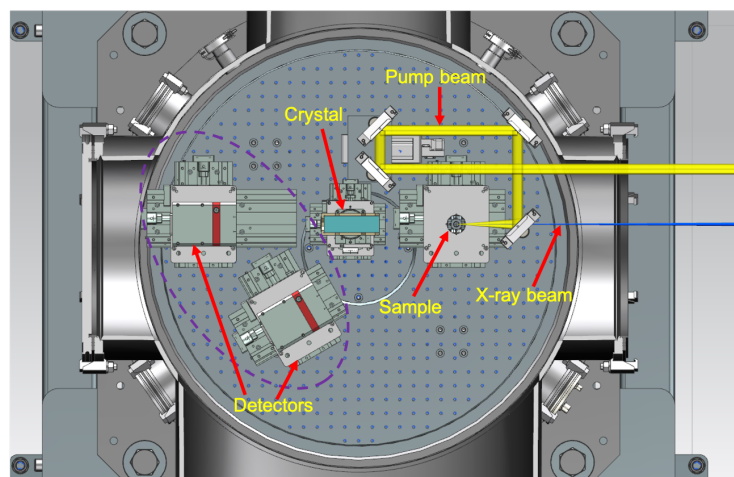

Figure 10. Schematic of the interior of the Gammatron user station, showing the setup for simultaneous time-resolved X-ray spectroscopy and diffraction experiments.

3.7. X-ray Source Parameters

Recent experimental findings using the several-hundred-terawatt-class driving laser show that $\sim 3 \times 10^{11}$ photons/s can be routinely generated in the Betatron scheme, and scaling laws [23] show that the photon flux can be further enhanced using PW-class driving lasers. Optimizing laser and plasma parameters can enhance the photon flux; for instance, using non-linear resonance of electrons in the cavity induced by multiple laser pulses will do so [44] or one can employ density-tailored targets generated by the blade or wire [45] obstructing the flow of a supersonic gas jet. With the PW class driver, a 10 Hz repetition rate, and optimized laser and target conditions, the laser-driven Betatron source will provide over 10^{11} photons per shot at the Gammatron beamline. The expected source parameters in Betatron and ICS schemes at the ELI Gammatron beamline are given in Table 2.

Table 2. Summary of X-ray source parameters expected at the Gammatron beamline, ELI Beamlines facility.

Parameters	Betatron	ICS
Energy range (keV)	5–200	100–20,000
Photon flux per shot	10^{11}	10^8–10^{10}
Bandwidth (%)	100	10–50
Peak Brightness	10^{25}	10^{23}
Photons in 0.1% BW	10^9	10^6
Beam divergence (mrad)	5–20	~10
Source size (μm)	<5	<5
Pulse duration (fs)	~10	~10
Repetition rate (Hz)	10	10

4. Applications of Gammatron Light Sources

The unique properties of Betatron and ICS X-ray sources, such as a micron-sized source, fs pulse duration, broadband spectrum, and photon flux over 10^{11} photons/shot, support the realization of various applications in atomic physics, biomolecular sciences, and in industrial applications [60]. Ultrafast time-resolved experiments can greatly benefit from such X-ray sources, as they are all-optical, have jitter-free synchronization of the pump pulse, and provide femtosecond temporal resolution in the pump-probe scheme. Furthermore, the large-energy tunability and possible narrow band of the ICS X-ray source can potentially be used in many applications in fundamental research and proof-of-concept industrial applications, including some in dense material radiography; non-destructive testing, screening, detection, and interdiction of special nuclear material; photo-fission; nuclear radiology; explosive detection; and low dose radiotherapy. Some of the potential applications which can be pursued at the Gammatron beamline are summarized below.

4.1. Applications of Betatron X-ray Source (5–150 keV)

Potential applications of the X-rays generated in the Gammatron beamline are broadly classified into X-ray imaging, time-resolved diffraction and spectroscopy, and industrial applications.

4.1.1. X-ray Imaging

(a) **X-ray phase-contrast imaging (XPCI)**: It is the most common imaging scheme performed with the partially coherent Betatron X-ray sources, as it offers superior contrast compared to the traditional absorption contrast imaging, specially for imaging specimens comprising lighter elements, such as soft biological tissues. The transverse coherence length of the X-ray source should be greater than $\frac{1}{2}\sqrt{\frac{\lambda D}{2}} \cong O$ (1–10 μm), where λ is the mean wavelength of the X-ray beam and D is the source-detector distance, to facilitate such imaging [61,62], which is met by Betatron sources owing to their small source size. A few instances of XPCI are already reported using Betatron sources [30,33,63,64]. The schematic scheme of XPCI and XPCI of a dry bee-fly using betatron source is shown in Figure 11. At the ELI Gammatron beamline, we will be able to generate Betatron radiation in the energy range of 10–200 keV and photon flux over 10^{11} photons per shot, which will be ideal for XPCI of biological samples with various thicknesses, given that 10–40 keV X-rays are used for soft-tissue absorption radiography (e.g., mammography) and 50–150 keV X-rays are used for harder-tissue (bone) radiography.
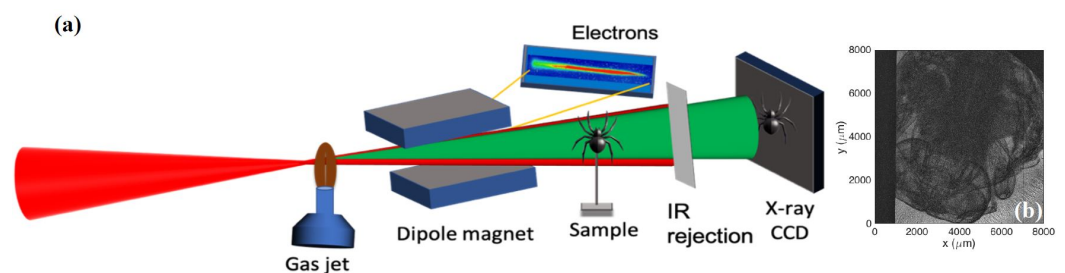

Figure 11. (**a**) Schematic of the propagation-based XPCI using a Betatron source. (**b**) XPCI of a dry bee-fly using a Betatron source.

Furthermore, short pulses and a high repetition rate allow motion freezing and time-lapse imaging, enabling real-time visualization of dynamics in the morphologies of biological samples (the respiration and circulatory system, the beating of a heart, etc.). Apart from the inline XPCI, it is also possible to perform speckle-based phase contrast imaging [65] and quantitative X-ray imaging techniques based on Talbot interferometry [66] using Betatron X-ray sources.

(b) **X-ray radiography and Microtomography**: Radiography and microtomography are important methods employed in archaeology, biomedical sciences (both in vitro and in vivo), developmental biology, electronics and microdevices, food and paleontology, and various other fields [67]. A Betatron X-ray source is ideal for high-resolution radiography. The micron source size allows high-resolution measurements by exploiting high geometric magnification and relaxing the resolution requirements of the detector. Additionally, the possibility of single-shot exposure owing to the high brightness of the Betatron source helps to avoid vibration-induced artifacts in measurements, which has been recently demonstrated [35,68].

(c) **Subsurface probing of high-energy-density (HED) state materials**: The laser-driven shock wave is an efficient way to generate dynamic high pressure for exploring the dynamical strengths of materials. Shocks are important in various fields of research, such as condensed matter physics, nuclear fusion, HED science [69–72], and laboratory astrophysics [73,74], as they provide the ability to test the extreme conditions of matter in terms of both pressure and temperature. This is extremely important in inertial confinement fusion research, where a series of shocks compress the fuel and capsules.

A high-power laser pulse can generate an ultrahigh pressure (tens of megabar to one gigabar) or mechanical shock inside the irradiated material locally [69–71], creating an extreme state of matter with high temperatures and densities that causes structural defects, local melting and fast recrystallization, phase transitions compositional inhomogeneities, etc. The laser-driven radiative shocks can be very dense ($n_e > 10^{21}$ cm^{-3}), and therefore, imaging these shocks requires a radiation source with high-energy photons to penetrate high-density plasmas, and sufficient brightness to overcome the plasma self-emission. High resolution subsurface probing is a key method for a real-time diagnosis of material behavior and inhomogeneities at the microscale. The Betatron X-ray sources have tremendous potential for applications in HED science, as they have remarkable spectral, spatial, and temporal properties. Due to their micron-scale source size, they possess significant spatial coherence, allowing the phase contrast imaging of the thin shock front. The intrinsic temporal resolution of the Betatron source is in the order of 10 fs, indicating that many ultrafast processes could be probed without motion blurring and/or compromising spatial resolution. A recent report demonstrated the ability of a Betatron source to image the laser-driven shock wave propagating in matter [37]. Imaging the shock propagation in matter using ultrafast X-ray provides a unique way to understand the material's failure mechanism and lattice defects with unprecedented resolution and provide real-time measurements of the microstructural evolution in the sample.

(d) **Quantum Imaging (QI)**: X-rays are ionizing radiation and hence can cause radiation damage to the specimen during the measurement. The damage in the specimen can be avoided by using the ultra-short pulsed X-ray sources, as proposed in the concept of "diffraction before destruction" [3]. Currently, such damage-free measurements are only possible with X-ray free-electron lasers; the other alternative to minimize the radiation-induced damage is low-dose imaging. The application of low-dose quantum imaging methods such as ghost imaging and interaction-free imaging has been well-demonstrated with visible light and recently with X-rays [75,76]. These methods are based on the intensity correlation of the reference beams and the object beam, as in the Hanbury Brown and Twiss interferometry experiments [77]. However, a major limiting factor in QI is the poor contrast of the images, which can be enhanced by employing femtosecond Betatron sources [78].

4.1.2. Time-Resolved X-ray Diffraction and Spectroscopy

Time-resolved X-ray diffraction and spectroscopy are the primary techniques employed to understand the transitional phenomena in material and biological sciences, which have atomic spatial resolution and temporal resolution in the order of tens of fem-

toseconds [79]. Time-resolved experiments with X-rays were predominantly performed with synchrotron X-rays. With the advent of X-ray free-electron lasers, improvement in the temporal resolution of the methods has been achieved [80]. Complementarily, compact femtosecond X-ray sources such as laser-driven K-alpha sources have also emerged for performing sub-picosecond X-ray diffraction and spectroscopy [81,82]. These in-house capabilities can be extended with the laser-driven Betatron X-rays, as they deliver pulses which last about ten femtoseconds. Using the Betatron source, all the initial transitional phenomena in chemical reactions, phase transition, lattice dynamics, vibrational motions, spin cross-over, and conical intersection can be probed. The broadband spectrum of the Betatron source is well suited for time-resolved X-ray absorption spectroscopy.

(a) **Time-resolved X-ray Diffraction**: X-ray diffraction is widely used for the structural characterization of materials and biological specimens. X-ray sources are used to provide structural details with atomic resolution. They can also reveal structural dynamics if they can deliver X-rays pulses. The picosecond time scale can be unravelled by the time-resolved experiments at synchrotrons. At the femtosecond time scale, such studies are performed with X-ray free-electron lasers, laser-driven K-alpha sources, and Betatron X-rays, and therefore, we foresee time-resolved diffraction as an important end-user experiment for the Gammatron beamline at ELI beamlines, with the possibility of the following measurements.

(i) Single Crystal X-ray Diffraction: It is the method of choice in both materials science and biological science to obtain the structure of a material. Ultrafast time-resolved X-ray studies of larger single crystals, especially in materials science, have been reported previously with laser-driven K-alpha sources by following the dynamics of the angular position or the intensity of Bragg peaks [83]. In biology, single crystal structural studies with laser-driven K-alpha source were reported [84]. However, the entire structure has never been revealed. Recently, a study showed that with a direct detector operated at a kilohertz frame rate and with the flux comparable to that from the laser-driven X-ray sources, structural studies of a single crystal of the sizes of ∼50 microns can be performed [85], which emphasizes the possibility to perform single-crystal Laue diffraction using the Betatron X-ray source at the Gammatron beamline.

(ii) Time-resolved powder diffraction: Crystals of both inorganic and organic molecules do not grow into sizes suitable for single crystal studies with traditional X-ray sources and hence are investigated either with X-ray free-electron lasers or with electrons [86]. Alternatively, structural studies of such small crystals can also be done with powder diffraction. Ultrafast time-resolved powder diffraction studies using various laser-driven X-ray sources have already been reported [87], proving the possibility of extending it at the Gammatron beamline too, making it a multi-functional user end station.

(iii) Time-resolved small angle and wide-angle scattering (SAXS/WAXS) of solutions: For the structural studies of small molecules and macromolecules, it is preferred that they are dissolved in solution rather than in the crystalline form. Probing the structure of molecules in solution with SAXS and WAXS is a standard operation at synchrotrons [88], and a recent report demonstrated SAXS/WAXS of biological macromolecules using laboratory sources with 10^6 photon/s [89]. This brings a bright perspective for the Betatron source to perform time-resolved structural studies of solutions which allow investigation of bond formation and breaking dynamics, ultrafast quakes in proteins, and several other structural transitions occurring at sub-picosecond timescales.

(b) **Time-resolved femtosecond X-ray absorption spectroscopy**: Time-resolved femtosecond X-ray spectroscopy has witnessed impressive growth and development in the past decade [90]. These developments have been specially powered by XFELs. The laser-driven X-ray sources have, however, played significant complementary roles in the development of these methods. The Betatron source has a short pulse duration

and a smooth broadband spectrum, which makes it an ideal source for time-resolved X-ray absorption spectroscopy.

(i) Time-resolved X-ray absorption spectroscopy (TR-XAS): Time-resolved X-ray absorption spectroscopy is a powerful tool in atomic physics, as it simultaneously reveals both electronic and atomic structures [91]. The X-ray absorption near-edge structure (XANES) and extended X-ray absorption fine structure (EXAFS) exploit a wide range of applications in chemistry, material science, studies of gas-phase systems, and/or complex biological samples. XAS has been extensively developed at synchrotrons, with X-ray energy in the range of 1–30 keV and a limited temporal resolution due to the duration of the synchrotron pulses ($\sim$10 ps). For most processes governed by atomic motion, such as structural changes and phase transitions, the timescale of interest corresponds to one vibrational period, i.e., $\approx$100 fs. XFEL sources are the most commonly used sources for TR-XAS experiments at the femtosecond time scale. However, the betatron source that gathers a broadband smooth spectrum and a femtosecond duration has been demonstrated to be as a powerful complementary source [92–94].

(ii) Time-resolved X-ray emission spectroscopy (TRXES): In addition to the information about the nature of bound ligands in a system [95], X-ray emission spectroscopy provides complementary information to X-ray absorption spectroscopy, on the electrons inside the specimen. TRXES has been demonstrated well with XFELs [96], and the broadband emission from Betatron sources can extend the capabilities of such investigations. The broadband Betatron sources can be efficiently used for simultaneous multi-excitation of the material, hence probing the charge and spin dynamics of both the light and heavy atoms inside the specimen, including both the valence and core electron dynamics.

(c) **Simultaneous time-resolved X-ray spectroscopy and diffraction**: Micron-sized ultrafast X-ray sources increase the flexibility of designing new tools for probing various samples, as in simultaneous time-resolved X-ray spectroscopy and diffraction. While X-ray spectroscopy provides information on the electronic, spin, and magnetization states, X-ray diffraction provides structural information. For photo-excited systems with non-radiative decay pathways, the system undergoes both electronic and structural transitions in tens of femtoseconds to picoseconds. Simultaneous measurement of X-ray spectrum and diffraction enables the probing of such systems and uncouples the electronic and structural transitions [97]. Additionally, this technique would benefit the probing of systems such as hemeproteins, where the association/dissociation of the ligands induces a change in the spin state and structural quakes in the system. The Gammatron beamline has prepared a user platform to provide this experimental capacity to the users.

4.1.3. Industrial Applications

The broadband energy spectrum and short pulse duration of the Betatron source makes it a lucrative source not only for fundamental studies but also for industrial applications [98]. An immediate application of this source would be the X-ray radiography of biomedical specimens. Conducting microtomography of bulk and composite materials, detecting the impurities and cracks, X-ray tomography, and spectroscopy of energy materials [99] are other applications of interest to the users from various industries. In battery systems, changes in the electrodes occur at picosecond timescales or lower, owing to the time scales of chemical reactions and/or charge transfer mechanisms occurring inside them. While recommending next-generation battery candidates (such as Li-S, which has an energy density of 2600 Whkg^{-1} compared to that of $\sim$600 Whkg^{-1} for Li-ion batteries) [100], these reactions and the degradation dynamics of the electrodes must be investigated in detail, as these are relevant to defining their charging cycles and hence their lifetimes [99]. Betatron X-rays at the Gammatron beamline can provide facilities for in operando X-ray computed tomography and time-resolved X-ray spectroscopy to investigate processes

mentioned above, contributing to the technologies supporting the development of new battery materials.

4.2. Applications of an Inverse-Compton Scattering X-ray Source (150 keV–20 MeV)

4.2.1. High-Resolution Industrial Imaging: X-ray Radiography/Tomography

The penetration of high energy X-rays into matter allows the investigation of bulk material, making hard X-ray and γ-ray radiography a widely used technique for non-destructive evaluation (NDE) via X-ray computed tomography (XCT) in various industrial applications. NDE is commonly used in manufacturing industries to assess design features and inspect the effects of mechanical testing and damage that occur over the service lifetime, as quality control is a key issue here. This includes the investigation of complex and large-sized products in aeronautics, and the development of new materials and manufacturing technologies. NDE, having high resolution in a short time, addresses challenges of the manufacturing industry such as inspecting full-scale parts, and the part experiences an extreme condition of heat and/or pressure, manufacturing tolerance in additive manufacturing for accurate metrology.

The state-of-the-art industrial NDE with high spatial resolution, fast scan speed, and element-specific analysis, is difficult to do with existing X-ray technology. The LPA-based X-ray sources capable of delivering extremely bright X-ray pulses have ideal properties for addressing these challenges. While their small source size allows for achieving excellent spatial resolution, their energy tunability could be beneficial to revealing the chemical composition of the sample via the K-edge subtraction method [101]. With this technique, scanning the object provides information about its component materials and its density. Projection-based imaging of dense objects using the all-optical ICS sources (photon energy up to 200 keV) has been demonstrated in the last decade [21,102], demonstrating also the single-shot imaging capability. The ICS source has also been used to demonstrate X-ray computed tomography of dense and complex objects [103]. With a low-divergence, high photon flux beam that operates at a high repetition rate (10 Hz), all-optical ICS X-ray sources at the Gammatron beamline will be ideal for performing the high-resolution radiography and tomography of dense objects in a short time. This source can be equally useful in proof-of-concept experiments related to the identification of long-range concealed objects by using the backscatter X-ray technique which is crucial in homeland security.

4.2.2. Nuclear Resonance Fluorescence (NRF)

Non-destructive detection and analysis of radioactive isotopes is one of the most critical issues for both the non-proliferation of nuclear materials and the nuclear waste management in the next generation of nuclear power plants. Non-destructive detection of radioactive isotopes could enable the fast and accurate assay of large amounts of nuclear wastes, reducing the cost dramatically and improving the quality of nuclear waste management. An MeV-class laser-driven ICS source can be an ideal probe for the non-destructive detection based on NRF, which is a process wherein a nucleus absorbs high-energy EM radiation and consequently emits a photon of slightly lower energy in order to attain equilibrium [104]. NRF provides a unique signature for each radioisotope of the nucleus of interest and gives information on energies of the excited states, their angular momenta, spin, parities, and their lifetimes, which are isotope-specific. Thus, the NRF is essential in the analysis of nuclear waste, stockpile stewardship, homeland security, and mining work. Since most of the nuclides have excitation states energy ranging from tens of kiloelectron volts to several megaelectron volts, a high energy X-ray or γ-ray source is indispensable for the NRF measurements. For instance, the nuclear fluorescence line of a light nucleon, i.e., lithium (^{7}Li), is 478 kiloelectron volts, whereas it is 16 MeV for a heavy radioactive nucleon, i.e., uranium (^{235}U). Recently, it was experimentally demonstrated that a Compton source can be a conventional accelerator, where the characteristic parameters of electrons can be tuned [105] and broadband bremsstrahlung sources [106] can excite NRF process. Hence, LPA-based X-ray sources are ideal to complement and/or replace the conventional NRF

sources. Although MeV photons are generated in a Betatron source [107], the X-rays from an ICS source are a more promising option, as they offer better energy tunability. Recent experimental studies using sophisticated electron injection, guiding, and focusing though a plasma lens showed that the bandwidth of electrons generated in LPA can be reduced under 1% [108]. An electron bunch with such a narrow energy spread, when interacting with a high-energy laser pulse, generates a narrow-bandwidth MeV-class ICS source. Such an LPA-driven ICS source demonstrated $\sim 10^8$ photons-s^{-1} within a 10% bandwidth at 13 MeV [109]. The ELI Gammatron beamline provides high photon flux in the energy range of hundreds of kiloelectron volts to several megaelectron volts, facilitating NRF investigations.

5. Conclusions and Perspectives

The Gammatron beamline, operating in two schemes, i.e, the Betatron scheme and the TS/ICS scheme, provides bright ultrashort pulses ranging from soft X-rays to γ-rays, which are relevant to realize a wide range of applications, as discussed in this report. While ultrashort broadband X-ray pulses with a spectral range from a few kiloelectron volts to few hundreds of kiloelectron volts are accessible in the Betatron scheme, a narrow band beam of hard X-rays with a spectral range of a few hundred kiloelectron volts to few megaelectron volts is available in the TS or ICS scheme. These X-ray/γ-rays can be precisely synchronized with the pump pulse (that is split from the main driving laser pulse), thereby facilitating time-resolved pump-probe experiments in a very broad range of photon energies with atomic resolution. These photon sources can be used to investigate the behavior of materials under extreme pressure and/or radiation conditions, having applications in the selection and development of materials for space engineering and fusion devices. In addition to the pump-probe studies, the Gammatron Beamline facilitates X-ray imaging, time-resolved diffraction, and spectroscopy experiments, thereby having wide applicability to physical sciences, chemical sciences, next-generation batteries, and biomedical and industrial applications.

Moreover, the polarization of the ICS source can be tuned by changing the polarization of the second laser beam. The polarized hard X-ray beam can be efficiently used in different applications such as magnetic microscopy [110], fluorescence imaging [96], and characterization of magnetic materials in nuclear physics research [111]. The ICS source at the Gammatron beamline will deliver a polarization tunable, quasi-monoenergetic, hard X-ray source ranging from a few kiloelectron volts to one megaelectron volt, providing a unique platform with which to test the magnetic materials.

ELI beamlines offer multiple lasers and bright, ultrashort X-ray pulses for user experiments. With multiple laser beams available in the Gammatron beamline, exploring extreme states created by laser-driven shock waves is possible with unprecedented spatio-temporal resolution. In addition to the Gammatron beamline, ELI Beamlines also offers a kJ-class long-pulse laser, L4n (1.8 kJ, 1 ns, 1 min/shot) [112], which can be employed for the investigation of matter under extreme conditions. Together with a bright, ultrafast hard-X-ray Betatron source [27], it is possible to exploit element-specific opacity measurements [113,114] in a high-repetition regime and for various laboratory astrophysics experiments at the ELI Plasma Physics Platform [115] as well.

Author Contributions: U.C. led the experimental design and wrote the original draft. M.L. performed LWFA PIC simulations. M.R. and K.H.R. performed the target characterization. K.P.K., K.T.-P., J.N., and S.V.B. provided input at all stages of the manuscript preparation. All authors have read and agreed to the published version of the manuscript.

Abbreviations

The following abbreviations are used in this manuscript:

ELI	Extreme Light Infrastructure
XFEL	X-ray Free-Electron Laser
fs	Femtosecond
HHG	High-order Harmonic Generation
LWFA	Laser Wakefield Acceleration
LPA	Laser Plasma Accelerator
TS	Thomson Scattering
ICS	Inverse Compton Scattering
HAPLS	High-Repetition-Rate Advanced Petawatt Laser System
DUHA	Dual-beam Ultra-fast High energy OPCPA Amplifier
PW	Pettawatt
OAP	Off-Axis Parabola
ES	Electron Spectrometer
ICT	Integrated Current Transformer
HAPG	Highly Annealed Pyrolytic Graphite
KB	Kirkpatrick-Baez
GaUS	Gammatron User Station
XPCI	X-ray phase-contrast imaging
HED	High Energy Density
QI	Quantum Imaging
SAXS	Small-Angle X-ray Scattering
WAXS	Wide-Angle X-ray Scattering
TR-XAS	Time-Resolved X-ray Absorption Spectroscopy
XANES	X-ray Absorption Near-Edge Structure
EXAFS	Extended X-ray Absorption Fine Structure
LCLS	Linac Coherent Light Source
WDM	Warm Dense Matter
TRXES	Time-Resolved X-ray Emission Spectroscopy
NDE	Non-Destructive Evaluation
NRF	Nuclear Resonance Fluorescence

References

1. Sakdinawat, A.; Attwood, D. Nanoscale X-ray imaging. *Nat. Photonics* **2010**, *4*, 840–848. [CrossRef]
2. Boutet, S.; Lomb, L.; Williams, G.J.; Barends, T.R.; Aquila, A.; Doak, R.B.; Weierstall, U.; DePonte, D.P.; Steinbrener, J.; Shoeman, R.L.; et al. High-resolution protein structure determination by serial femtosecond crystallography. *Science* **2012**, *337*, 362–364. [CrossRef] [PubMed]
3. Neutze, R.; Wouts, R.; Van der Spoel, D.; Weckert, E.; Hajdu, J. Potential for biomolecular imaging with femtosecond X-ray pulses. *Nature* **2000**, *406*, 752–757. [CrossRef] [PubMed]
4. Chapman, H.N.; Fromme, P.; Barty, A.; White, T.A.; Kirian, R.A.; Aquila, A.; Hunter, M.S.; Schulz, J.; DePonte, D.P.; Weierstall, U.; et al. Femtosecond X-ray protein nanocrystallography. *Nature* **2011**, *470*, 73–77. [CrossRef]

5. Schoenlein, R.W.; Leemans, W.; Chin, A.; Volfbeyn, P.; Glover, T.; Balling, P.; Zolotorev, M.; Kim, K.J.; Chattopadhyay, S.; Shank, C. Femtosecond X-ray pulses at 0.4 Å generated by 90 Thomson scattering: A tool for probing the structural dynamics of materials. *Science* **1996**, *274*, 236–238. [CrossRef]
6. Cavalleri, A.; Tóth, C.; Siders, C.W.; Squier, J.; Ráksi, F.; Forget, P.; Kieffer, J. Femtosecond structural dynamics in VO$_2$ during an ultrafast solid–solid phase transition. *Phys. Rev. Lett.* **2001**, *87*, 237401. [CrossRef] [PubMed]
7. Tajima, T.; Malka, V. Laser plasma accelerators. *Plasma Phys. Control. Fusion* **2020**, *62*, 034004. [CrossRef]
8. Gaarde, M.B.; Tate, J.L.; Schafer, K.J. Macroscopic aspects of attosecond pulse generation. *J. Phys. B At. Mol. Opt. Phys.* **2008**, *41*, 132001. [CrossRef]
9. Li, J.; Ren, X.; Yin, Y.; Zhao, K.; Chew, A.; Cheng, Y.; Cunningham, E.; Wang, Y.; Hu, S.; Wu, Y.; et al. 53-attosecond X-ray pulses reach the carbon K-edge. *Nat. Commun.* **2017**, *8*, 1–5. [CrossRef]
10. Hort, O.; Albrecht, M.; Nefedova, V.E.; Finke, O.; Mai, D.; Reyné, S.; Giambruno, F.; Frassetto, F.; Poletto, L.; Andreasson, J.; et al. High-flux source of coherent XUV pulses for user applications. *Opt. Express* **2019**, *27*, 8871–8883. [CrossRef]
11. Makos, I.; Orfanos, I.; Nayak, A.; Peschel, J.; Major, B.; Liontos, I.; Skantzakis, E.; Papadakis, N.; Kalpouzos, C.; Dumergue, M.; et al. A 10-gigawatt attosecond source for non-linear XUV optics and XUV-pump-XUV-probe studies. *Sci. Rep.* **2020**, *10*, 3759. [CrossRef] [PubMed]
12. Schötz, J.; Förg, B.; Schweinberger, W.; Liontos, I.; Masood, H.; Kamal, A.; Jakubeit, C.; Kling, N.; Paasch-Colberg, T.; Biswas, S.; et al. Phase-matching for generation of isolated attosecond xuv and soft-X-ray pulses with few-cycle drivers. *Phys. Rev. X* **2020**, *10*, 041011. [CrossRef]
13. Tajima, T.; Dawson, J.M. Laser electron accelerator. *Phys. Rev. Lett.* **1979**, *43*, 267. [CrossRef]
14. Leemans, W.; Gonsalves, A.; Mao, H.S.; Nakamura, K.; Benedetti, C.; Schroeder, C.; Tóth, C.; Daniels, J.; Mittelberger, D.; Bulanov, S.; et al. Multi-GeV electron beams from capillary-discharge-guided subpetawatt laser pulses in the self-trapping regime. *Phys. Rev. Lett.* **2014**, *113*, 245002. [CrossRef]
15. Gonsalves, A.; Nakamura, K.; Daniels, J.; Benedetti, C.; Pieronek, C.; De Raadt, T.; Steinke, S.; Bin, J.; Bulanov, S.; Van Tilborg, J.; et al. Petawatt laser guiding and electron beam acceleration to 8 GeV in a laser-heated capillary discharge waveguide. *Phys. Rev. Lett.* **2019**, *122*, 084801. [CrossRef]
16. Rousse, A.; Phuoc, K.T.; Shah, R.; Pukhov, A.; Lefebvre, E.; Malka, V.; Kiselev, S.; Burgy, F.; Rousseau, J.P.; Umstadter, D.; et al. Production of a keV X-ray beam from synchrotron radiation in relativistic laser-plasma interaction. *Phys. Rev. Lett.* **2004**, *93*, 135005. [CrossRef]
17. Ta Phuoc, K.; Fitour, R.; Tafzi, A.; Garl, T.; Artemiev, N.; Shah, R.; Albert, F.; Boschetto, D.; Rousse, A.; Kim, D.; et al. Demonstration of the ultrafast nature of laser produced betatron radiation. *Phys. Plasmas* **2007**, *14*, 080701. [CrossRef]
18. Corde, S.; Phuoc, K.T.; Lambert, G.; Fitour, R.; Malka, V.; Rousse, A.; Beck, A.; Lefebvre, E. Femtosecond x rays from laser-plasma accelerators. *Rev. Mod. Phys.* **2013**, *85*, 1. [CrossRef]
19. Ta Phuoc, K.; Corde, S.; Thaury, C.; Malka, V.; Tafzi, A.; Goddet, J.P.; Shah, R.; Sebban, S.; Rousse, A. All-optical Compton gamma-ray source. *Nat. Photonics* **2012**, *6*, 308–311. [CrossRef]
20. Chen, S.; Powers, N.; Ghebregziabher, I.; Maharjan, C.; Liu, C.; Golovin, G.; Banerjee, S.; Zhang, J.; Cunningham, N.; Moorti, A.; et al. MeV-energy X rays from inverse Compton scattering with laser-wakefield accelerated electrons. *Phys. Rev. Lett.* **2013**, *110*, 155003. [CrossRef]
21. Maier, A.R.; Delbos, N.M.; Eichner, T.; Hübner, L.; Jalas, S.; Jeppe, L.; Jolly, S.W.; Kirchen, M.; Leroux, V.; Messner, P.; et al. Decoding sources of energy variability in a laser-plasma accelerator. *Phys. Rev. X* **2020**, *10*, 031039. [CrossRef]
22. Corde, S.; Phuoc, K.T.; Fitour, R.; Faure, J.; Tafzi, A.; Goddet, J.P.; Malka, V.; Rousse, A. Controlled betatron X-ray radiation from tunable optically injected electrons. *Phys. Rev. Lett.* **2011**, *107*, 255003. [CrossRef] [PubMed]
23. Fourmaux, S.; Hallin, E.; Chaulagain, U.; Weber, S.; Kieffer, J. Laser-based synchrotron X-ray radiation experimental scaling. *Opt. Express* **2020**, *28*, 3147–3158. [CrossRef] [PubMed]
24. Mourou, G.A.; Korn, G.; Sandner, W.; Collier, J.L. *Eli-Extreme Light Infrastructure: Science and Technology with Ultra-Intense Lasers, Whitebook*; THOSS Media GmbH: Berlin, Germany, 2011.
25. ELI Beamlines—Dolní Břežany. Available online: https://www.eli-beams.eu/ (accessed on 7 November 2022).
26. Nejdl, J.; Mai, D.D.; Chaulagain, U.; Hort, O.; Finke, O.; Albrecht, M.; Jurkovič, M.; Lera, R.; Karatodorov, S.; Lamač, M.; et al. Progress on laser-driven X-ray sources at ELI Beamlines. In Proceedings of the X-ray Lasers and Coherent X-ray Sources: Development and Applications XIII, San Diego, CA, USA, 12–13 August 2019; Volume 11111, pp. 44–50.
27. Chaulagain, U.; Boháček, K.; Vančura, J.; Lamač, M.; Yan, W.; Gu, Y.; Kozlová, M.; Ta-Phuoc, K.; Weber, S.; Nejdl, J. LWFA-driven betatron source for Plasma Physics Platform at ELI Beamlines. In Proceedings of the International Conference on X-ray Lasers, Prague, Czech Republic, 7–12 October 2018; pp. 117–123.
28. Margarone, D.; Cirrone, G.P.; Cuttone, G.; Amico, A.; Andò, L.; Borghesi, M.; Bulanov, S.S.; Bulanov, S.V.; Chatain, D.; Fajstavr, A.; et al. ELIMAIA: A laser-driven ion accelerator for multidisciplinary applications. *Quantum Beam Sci.* **2018**, *2*, 8. [CrossRef]
29. Sarri, G.; Corvan, D.; Schumaker, W.; Cole, J.; Di Piazza, A.; Ahmed, H.; Harvey, C.; Keitel, C.H.; Krushelnick, K.; Mangles, S.; et al. Ultrahigh brilliance multi-MeV γ-ray beams from nonlinear relativistic Thomson scattering. *Phys. Rev. Lett.* **2014**, *113*, 224801. [CrossRef]

30. Kneip, S.; McGuffey, C.; Dollar, F.; Bloom, M.; Chvykov, V.; Kalintchenko, G.; Krushelnick, K.; Maksimchuk, A.; Mangles, S.; Matsuoka, T.; et al. X-ray phase contrast imaging of biological specimens with femtosecond pulses of betatron radiation from a compact laser plasma wakefield accelerator. *Appl. Phys. Lett.* **2011**, *99*, 093701. [CrossRef]

31. Ju, J.; Svensson, K.; Döpp, A.; Ferrari, H.; Cassou, K.; Neveu, O.; Genoud, G.; Wojda, F.; Burza, M.; Persson, A.; et al. Enhancement of X-rays generated by a guided laser wakefield accelerator inside capillary tubes. *Appl. Phys. Lett.* **2012**, *100*, 191106. [CrossRef]

32. Wang, X.; Zgadzaj, R.; Fazel, N.; Li, Z.; Yi, S.; Zhang, X.; Henderson, W.; Chang, Y.Y.; Korzekwa, R.; Tsai, H.E.; et al. Quasi-monoenergetic laser-plasma acceleration of electrons to 2 GeV. *Nat. Commun.* **2013**, *4*, 1988. [CrossRef]

33. Wenz, J.; Schleede, S.; Khrennikov, K.; Bech, M.; Thibault, P.; Heigoldt, M.; Pfeiffer, F.; Karsch, S. Quantitative X-ray phase-contrast microtomography from a compact laser-driven betatron source. *Nat. Commun.* **2015**, *6*, 7568. [CrossRef]

34. Chen, L.; Yan, W.; Li, D.; Hu, Z.; Zhang, L.; Wang, W.; Hafz, N.; Mao, J.; Huang, K.; Ma, Y.; et al. Bright betatron X-ray radiation from a laser-driven-clustering gas target. *Sci. Rep.* **2013**, *3*, 1912. [CrossRef]

35. Cole, J.; Wood, J.; Lopes, N.; Poder, K.; Abel, R.; Alatabi, S.; Bryant, J.; Jin, A.; Kneip, S.; Mecseki, K.; et al. Laser-wakefield accelerators as hard X-ray sources for 3D medical imaging of human bone. *Sci. Rep.* **2015**, *5*, 13244. [CrossRef] [PubMed]

36. Döpp, A.; Mahieu, B.; Lifschitz, A.; Thaury, C.; Doche, A.; Guillaume, E.; Grittani, G.; Lundh, O.; Hansson, M.; Gautier, J.; et al. Stable femtosecond X-rays with tunable polarization from a laser-driven accelerator. *Light. Sci. Appl.* **2017**, *6*, e17086. [CrossRef] [PubMed]

37. Wood, J.; Chapman, D.; Poder, K.; Lopes, N.; Rutherford, M.; White, T.; Albert, F.; Behm, K.; Booth, N.; Bryant, J.; et al. Ultrafast imaging of laser driven shock waves using betatron X-rays from a laser wakefield accelerator. *Sci. Rep.* **2018**, *8*, 11010. [CrossRef] [PubMed]

38. Fourmaux, S.; Hallin, E.; Arnison, P.; Kieffer, J. Optimization of laser-based synchrotron X-ray for plant imaging. *Appl. Phys. B* **2019**, *125*, 1–9. [CrossRef]

39. Tsung, F.S.; Narang, R.; Mori, W.B.; Joshi, C.; Fonseca, R.; Silva, L.O. Near-GeV-energy laser-wakefield acceleration of self-injected electrons in a centimeter-scale plasma channel. *Phys. Rev. Lett.* **2004**, *93*, 185002. [CrossRef]

40. Bulanov, S.; Kirsanov, V.; Sakharov, A. Limiting electric field of the wakefield plasma wave. *JETP Lett.* **1991**, *53*, 565–569.

41. Modena, A.; Najmudin, Z.; Dangor, A.; Clayton, C.; Marsh, K.; Joshi, C.; Malka, V.; Darrow, C.; Danson, C.; Neely, D.; et al. Electron acceleration from the breaking of relativistic plasma waves. *Nature* **1995**, *377*, 606–608. [CrossRef]

42. Jackson, J.D. *Classical Electrodynamics*, 3rd ed.; John Wiley & Sons: New York, NY, USA, 1999.

43. Thaury, C.; Guillaume, E.; Döpp, A.; Lehe, R.; Lifschitz, A.; Ta Phuoc, K.; Gautier, J.; Goddet, J.P.; Tafzi, A.; Flacco, A.; et al. Demonstration of relativistic electron beam focusing by a laser-plasma lens. *Nat. Commun.* **2015**, *6*, 6860. [CrossRef]

44. Lamač, M.; Chaulagain, U.; Jurkovič, M.; Nejdl, J.; Bulanov, S. Two-color nonlinear resonances in betatron oscillations of laser accelerated relativistic electrons. *Phys. Rev. Res.* **2021**, *3*, 033088. [CrossRef]

45. Kozlova, M.; Andriyash, I.; Gautier, J.; Sebban, S.; Smartsev, S.; Jourdain, N.; Chaulagain, U.; Azamoum, Y.; Tafzi, A.; Goddet, J.P.; et al. Hard X rays from laser-wakefield accelerators in density tailored plasmas. *Phys. Rev. X* **2020**, *10*, 011061. [CrossRef]

46. Björklund S, J.; Guénot, D.; Ferri, J.; Ekerfelt, H.; Gallardo González, I.; Persson, A.; Svendsen, K.; Veisz, L.; Lundh, O. Low-divergence femtosecond X-ray pulses from a passive plasma lens. *Nat. Phys.* **2021**, *17*, 639–645. [CrossRef]

47. Green, J.T.; Antipenkov, R.; Bakule, P. L2-DUHA 100 TW high repetition rate laser system at ELI-Beamlines. Key design considerations. *Rev. Laser Eng.* **2021**, *49*, 106–109.

48. Willemsen, T.; Chaulagain, U.; Havlíčková, I.; Borneis, S.; Ebert, W.; Ehlers, H.; Gauch, M.; Groß, T.; Kramer, D.; Laštovička, T.; et al. Large area ion beam sputtered dielectric ultrafast mirrors for petawatt laser beamlines. *Opt. Express* **2022**, *30*, 6129–6141. [CrossRef] [PubMed]

49. Borneis, S.; Laštovička, T.; Sokol, M.; Jeong, T.M.; Condamine, F.; Renner, O.; Tikhonchuk, V.; Bohlin, H.; Fajstavr, A.; Hernandez, J.C.; et al. Design, installation and commissioning of the ELI-Beamlines high-power, high-repetition rate HAPLS laser beam transport system to P3. *High Power Laser Sci. Eng.* **2021**, *9*, E30. [CrossRef]

50. McGuffey, C.; Thomas, A.; Schumaker, W.; Matsuoka, T.; Chvykov, V.; Dollar, F.; Kalintchenko, G.; Yanovsky, V.; Maksimchuk, A.; Krushelnick, K.; et al. Ionization induced trapping in a laser wakefield accelerator. *Phys. Rev. Lett.* **2010**, *104*, 025004. [CrossRef] [PubMed]

51. Huang, K.; Li, D.; Yan, W.; Li, M.; Tao, M.; Chen, Z.; Ge, X.; Liu, F.; Ma, Y.; Zhao, J.; et al. Simultaneous generation of quasi-monoenergetic electron and betatron X-rays from nitrogen gas via ionization injection. *Appl. Phys. Lett.* **2014**, *105*, 204101. [CrossRef]

52. Boháček, K.; Kozlová, M.; Nejdl, J.; Chaulagain, U.; Hornỳ, V.; Krus, M.; Phuoc, K.T. Stable electron beams from laser wakefield acceleration with few-terawatt driver using a supersonic air jet. *Nucl. Instrum. Methods Phys. Res. Sect. A Accel. Spectrometers Detect. Assoc. Equip.* **2018**, *883*, 24–28. [CrossRef]

53. Bulanov, S.; Naumova, N.; Pegoraro, F.; Sakai, J. Particle injection into the wave acceleration phase due to nonlinear wake wave breaking. *Phys. Rev. E* **1998**, *58*, R5257. [CrossRef]

54. Nejdl, J.; Vančura, J.; Boháček, K.; Albrecht, M.; Chaulagain, U. Imaging Michelson interferometer for a low-density gas jet characterization. *Rev. Sci. Instrum.* **2019**, *90*, 065107. [CrossRef]

55. Chaulagain, U.; Karatodorov, S.; Raclavskỳ, M.; Lorenz, S.; Lamač, M.; Albrecht, M.; Tomkus, V.; Dudutis, J.; Mackevičiūtė, M.; Gečys, P.; et al. Tomographic characterization of gas jets for laser-plasma acceleration with increased sensitivity. In Proceedings of the International Conference on X-ray Lasers 2020, Online, 8–10 October 2020; Volume 11886, pp. 61–67.

56. Karatodorov, S.; Lera, R.; Raclavsky, M.; Lorenz, S.; Chaulagain, U.; Nejdl, J. Multi-pass probing for high-sensitivity tomographic interferometry. *Sci. Rep.* **2021**, *11*, 15072. [CrossRef]

57. Glinec, Y.; Faure, J.; Guemnie-Tafo, A.; Malka, V.; Monard, H.; Larbre, J.; De Waele, V.; Marignier, J.; Mostafavi, M. Absolute calibration for a broad range single shot electron spectrometer. *Rev. Sci. Instrum.* **2006**, *77*, 103301. [CrossRef]

58. Kettle, B.; Gerstmayr, E.; Streeter, M.; Albert, F.; Baggott, R.; Bourgeois, N.; Cole, J.; Dann, S.; Falk, K.; González, I.G.; et al. Single-shot multi-keV X-ray absorption spectroscopy using an ultrashort laser-wakefield accelerator source. *Phys. Rev. Lett.* **2019**, *123*, 254801. [CrossRef] [PubMed]

59. Raclavský, M.; Khakurel, K.P.; Chaulagain, U.; Lamač, M.; Nejdl, J. Multi-Lane Mirror for Broadband Applications of the Betatron X-ray Source. *Photonics* **2021**, *8*, 579. [CrossRef]

60. Albert, F.; Thomas, A.G. Applications of laser wakefield accelerator-based light sources. *Plasma Phys. Control. Fusion* **2016**, *58*, 103001. [CrossRef]

61. Davis, T.J.; Gao, D.; Gureyev, T.; Stevenson, A.; Wilkins, S. Phase-contrast imaging of weakly absorbing materials using hard X-rays. *Nature* **1995**, *373*, 595–598. [CrossRef]

62. Wilkins, S.; Gureyev, T.E.; Gao, D.; Pogany, A.; Stevenson, A. Phase-contrast imaging using polychromatic hard X-rays. *Nature* **1996**, *384*, 335–338. [CrossRef]

63. Fourmaux, S.; Corde, S.; Phuoc, K.T.; Lassonde, P.; Lebrun, G.; Payeur, S.; Martin, F.; Sebban, S.; Malka, V.; Rousse, A.; et al. Single shot phase contrast imaging using laser-produced Betatron X-ray beams. *Opt. Lett.* **2011**, *36*, 2426–2428. [CrossRef]

64. Chaulagain, U.; Bohacek, K.; Kozlova, M.; Nejdl, J.; Krus, M.; Horny, V.; Mahieu, B.; Ta-Phuoc, K. X-ray phase contrast imaging of biological samples using a betatron X-ray source generated in a laser wakefield accelerator. In Proceedings of the Laser Acceleration of Electrons, Protons, and Ions IV, Prague, Czech Republic, 24–26 April 2017; Volume 10240, pp. 110–114.

65. Zdora, M.C. State of the art of X-ray speckle-based phase-contrast and dark-field imaging. *J. Imaging* **2018**, *4*, 60. [CrossRef]

66. Momose, A.; Yashiro, W.; Harasse, S.; Kuwabara, H. Four-dimensional X-ray phase tomography with Talbot interferometry and white synchrotron radiation: Dynamic observation of a living worm. *Opt. Express* **2011**, *19*, 8423–8432. [CrossRef]

67. Landis, E.N.; Keane, D.T. X-ray microtomography. *Mater. Charact.* **2010**, *61*, 1305–1316. [CrossRef]

68. Döpp, A.; Hehn, L.; Götzfried, J.; Wenz, J.; Gilljohann, M.; Ding, H.; Schindler, S.; Pfeiffer, F.; Karsch, S. Quick X-ray microtomography using a laser-driven betatron source. *Optica* **2018**, *5*, 199–203. [CrossRef]

69. Suzuki-Vidal, F.; Clayson, T.; Stehlé, C.; Swadling, G.; Foster, J.; Skidmore, J.; Graham, P.; Burdiak, G.; Lebedev, S.; Chaulagain, U.; et al. Counterpropagating radiative shock experiments on the orion laser. *Phys. Rev. Lett.* **2017**, *119*, 055001. [CrossRef] [PubMed]

70. Ping, Y.; Coppari, F.; Hicks, D.; Yaakobi, B.; Fratanduono, D.; Hamel, S.; Eggert, J.; Rygg, J.; Smith, R.; Swift, D.; et al. Solid iron compressed up to 560 GPa. *Phys. Rev. Lett.* **2013**, *111*, 065501. [CrossRef] [PubMed]

71. Tsujino, M.; Sano, T.; Sakata, O.; Ozaki, N.; Kimura, S.; Takeda, S.; Okoshi, M.; Inoue, N.; Kodama, R.; Kobayashi, K.F.; et al. Synthesis of submicron metastable phase of silicon using femtosecond laser-driven shock wave. *J. Appl. Phys.* **2011**, *110*, 126103.

72. Suzuki-Vidal, F.; Clayson, T.; Stehlé, C.; Chaulagain, U.; Halliday, J.W.; Sun, M.; Ren, L.; Kang, N.; Liu, H.; Zhu, B.; et al. First radiative shock experiments on the SG-II laser. *High Power Laser Sci. Eng.* **2021**, *9*, E27. [CrossRef]

73. Singh, R.; Stehlé, C.; Suzuki-Vidal, F.; Kozlova, M.; Larour, J.; Chaulagain, U.; Clayson, T.; Rodriguez, R.; Gil, J.; Nejdl, J.; et al. Experimental study of the interaction of two laser-driven radiative shocks at the PALS laser. *High Energy Density Phys.* **2017**, *23*, 20–30. [CrossRef]

74. Chaulagain, U.; Stehlé, C.; Larour, J.; Kozlová, M.; Suzuki-Vidal, F.; Barroso, P.; Cotelo, M.; Velarde, P.; Rodriguez, R.; Gil, J.; et al. Structure of a laser-driven radiative shock. *High Energy Density Phys.* **2015**, *17*, 106–113. [CrossRef]

75. Pelliccia, D.; Rack, A.; Scheel, M.; Cantelli, V.; Paganin, D.M. Experimental X-ray Ghost Imaging. *Phys. Rev. Lett.* **2016**, *117*, 113902. [CrossRef]

76. Zhang, A.X.; He, Y.H.; Wu, L.A.; Chen, L.M.; Wang, B.B. Tabletop X-ray ghost imaging with ultra-low radiation. *Optica* **2018**, *5*, 374–377. [CrossRef]

77. Brown, R.H.; Twiss, R.Q. LXXIV. A new type of interferometer for use in radio astronomy. *Lond. Edinb. Dublin Philos. Mag. J. Sci.* **1954**, *45*, 663–682. [CrossRef]

78. Kim, Y.Y.; Gelisio, L.; Mercurio, G.; Dziarzhytski, S.; Beye, M.; Bocklage, L.; Classen, A.; David, C.; Gorobtsov, O.Y.; Khubbutdinov, R.; et al. Ghost imaging at an XUV free-electron laser. *Phys. Rev. A* **2020**, *101*, 013820. [CrossRef]

79. Chergui, M.; Collet, E. Photoinduced structural dynamics of molecular systems mapped by time-resolved X-ray methods. *Chem. Rev.* **2017**, *117*, 11025–11065. [CrossRef] [PubMed]

80. Neutze, R.; Moffat, K. Time-resolved structural studies at synchrotrons and X-ray free electron lasers: Opportunities and challenges. *Curr. Opin. Struct. Biol.* **2012**, *22*, 651–659. [CrossRef] [PubMed]

81. Afshari, M.; Krumey, P.; Menn, D.; Nicoul, M.; Brinks, F.; Tarasevitch, A.; Sokolowski-Tinten, K. Time-resolved diffraction with an optimized short pulse laser plasma X-ray source. *Struct. Dyn.* **2020**, *7*, 014301. [CrossRef] [PubMed]

82. Anwar, M.; Iqbal, M.; Hwang, B.; Faiyaz, M.; Mun, B.; Janulewicz, K.; Noh, D. Ultrafast X-ray absorption near edge spectroscopy of Fe_3O_4 using a laboratory based femtosecond X-ray source. *Opt. Express* **2019**, *27*, 6030–6036. [CrossRef] [PubMed]

83. Sokolowski-Tinten, K.; Blome, C.; Blums, J.; Cavalleri, A.; Dietrich, C.; Tarasevitch, A.; Uschmann, I.; Förster, E.; Kammler, M.; Horn-von Hoegen, M.; et al. Femtosecond X-ray measurement of coherent lattice vibrations near the Lindemann stability limit. *Nature* **2003**, *422*, 287–289. [CrossRef]

84. Bonvalet, A.; Darmon, A.; Lambry, J.C.; Martin, J.L.; Audebert, P. 1 kHz tabletop ultrashort hard X-ray source for time-resolved X-ray protein crystallography. *Opt. Lett.* **2006**, *31*, 2753–2755. [CrossRef]

85. Khakurel, K.P.; Espinoza, S.; Savko, M.; Polovinkin, V.; Dohnalek, J.; Shepard, W.; Angelova, A.; Hajdu, J.; Andreasson, J.; Angelov, B. Kilohertz Macromolecular Crystallography Using an EIGER Detector at Low X-ray Fluxes. *Crystals* **2020**, *10*, 1146. [CrossRef]

86. Khakurel, K.P.; Angelov, B.; Andreasson, J. Macromolecular nanocrystal structural analysis with electron and X-rays: A comparative review. *Molecules* **2019**, *24*, 3490. [CrossRef]

87. Zamponi, F.; Ansari, Z.; Wörner, M.; Elsaesser, T. Femtosecond powder diffraction with a laser-driven hard X-ray source. *Opt. Express* **2010**, *18*, 947–961. [CrossRef]

88. Graewert, M.A.; Svergun, D.I. Impact and progress in small and wide angle X-ray scattering (SAXS and WAXS). *Curr. Opin. Struct. Biol.* **2013**, *23*, 748–754. [CrossRef] [PubMed]

89. Bruetzel, L.K.; Fischer, S.; Salditt, A.; Sedlak, S.M.; Nickel, B.; Lipfert, J. A Mo-anode-based in-house source for small-angle X-ray scattering measurements of biological macromolecules. *Rev. Sci. Instrum.* **2016**, *87*, 025103. [CrossRef] [PubMed]

90. Chergui, M. Time-resolved X-ray spectroscopies of chemical systems: New perspectives. *Struct. Dyn.* **2016**, *3*, 031001. [CrossRef] [PubMed]

91. Bressler, C.; Chergui, M. Molecular structural dynamics probed by ultrafast X-ray absorption spectroscopy. *Annu. Rev. Phys. Chem.* **2010**, *61*, 263–282. [CrossRef]

92. Mo, M.; Chen, Z.; Fourmaux, S.; Saraf, A.; Otani, K.; Kieffer, J.; Tsui, Y.; Ng, A.; Fedosejevs, R. Laser wakefield generated X-ray probe for femtosecond time-resolved measurements of ionization states of warm dense aluminum. *Rev. Sci. Instrum.* **2013**, *84*, 123106. [CrossRef]

93. Mahieu, B.; Jourdain, N.; Ta Phuoc, K.; Dorchies, F.; Goddet, J.P.; Lifschitz, A.; Renaudin, P.; Lecherbourg, L. Probing warm dense matter using femtosecond X-ray absorption spectroscopy with a laser-produced betatron source. *Nat. Commun.* **2018**, *9*, 3276. [CrossRef] [PubMed]

94. Grolleau, A.; Dorchies, F.; Jourdain, N.; Phuoc, K.T.; Gautier, J.; Mahieu, B.; Renaudin, P.; Recoules, V.; Martinez, P.; Lecherbourg, L. Femtosecond Resolution of the Nonballistic Electron Energy Transport in Warm Dense Copper. *Phys. Rev. Lett.* **2021**, *127*, 275901. [CrossRef]

95. De Groot, F. High-resolution X-ray emission and X-ray absorption spectroscopy. *Chem. Rev.* **2001**, *101*, 1779–1808. [CrossRef]

96. Pushkar, Y.; Long, X.; Glatzel, P.; Brudvig, G.W.; Dismukes, G.C.; Collins, T.J.; Yachandra, V.K.; Yano, J.; Bergmann, U. Direct Detection of Oxygen Ligation to the Mn4Ca Cluster of Photosystem II by X-ray Emission Spectroscopy. *Angew. Chem. Int. Ed.* **2010**, *49*, 800–803. [CrossRef]

97. Kern, J.; Alonso-Mori, R.; Tran, R.; Hattne, J.; Gildea, R.J.; Echols, N.; Glöckner, C.; Hellmich, J.; Laksmono, H.; Sierra, R.G.; et al. Simultaneous femtosecond X-ray spectroscopy and diffraction of photosystem II at room temperature. *Science* **2013**, *340*, 491–495. [CrossRef]

98. Gruse, J.N.; Streeter, M.; Thornton, C.; Armstrong, C.; Baird, C.; Bourgeois, N.; Cipiccia, S.; Finlay, O.; Gregory, C.; Katzir, Y.; et al. Application of compact laser-driven accelerator X-ray sources for industrial imaging. *Nucl. Instrum. Methods Phys. Res. Sect. A Accel. Spectrometers Detect. Assoc. Equip.* **2020**, *983*, 164369. [CrossRef]

99. Shearing, P.; Wu, Y.; Harris, S.J.; Brandon, N. In situ X-ray spectroscopy and imaging of battery materials. *Electrochem. Soc. Interface* **2011**, *20*, 43. [CrossRef]

100. Sun, K.; Zhao, C.; Lin, C.H.; Stavitski, E.; Williams, G.J.; Bai, J.; Dooryhee, E.; Attenkofer, K.; Thieme, J.; Chen-Wiegart, Y.c.K.; et al. Operando multi-modal synchrotron investigation for structural and chemical evolution of cupric sulfide (CuS) additive in Li-S battery. *Sci. Rep.* **2017**, *7*, 12976. [CrossRef] [PubMed]

101. Kulpe, S.; Dierolf, M.; Günther, B.; Busse, M.; Achterhold, K.; Gleich, B.; Herzen, J.; Rummeny, E.; Pfeiffer, F.; Pfeiffer, D. K-edge subtraction computed tomography with a compact synchrotron X-ray source. *Sci. Rep.* **2019**, *9*, 13332. [CrossRef] [PubMed]

102. Döpp, A.; Guillaume, E.; Thaury, C.; Gautier, J.; Andriyash, I.; Lifschitz, A.; Malka, V.; Rousse, A.; Phuoc, K.T. An all-optical Compton source for single-exposure X-ray imaging. *Plasma Phys. Control. Fusion* **2016**, *58*, 034005. [CrossRef]

103. Ma, Y.; Hua, J.; Liu, D.; He, Y.; Zhang, T.; Chen, J.; Yang, F.; Ning, X.; Yang, Z.; Zhang, J.; et al. Region-of-interest micro-focus computed tomography based on an all-optical inverse Compton scattering source. *Matter Radiat. Extrem.* **2020**, *5*, 064401. [CrossRef]

104. Hajima, R.; Hayakawa, T.; Kikuzawa, N.; Minehara, E. Proposal of nondestructive radionuclide assay using a high-flux gamma-ray source and nuclear resonance fluorescence. *J. Nucl. Sci. Technol.* **2008**, *45*, 441–451. [CrossRef]

105. Kikuzawa, N.; Hajima, R.; Nishimori, N.; Minehara, E.; Hayakawa, T.; Shizuma, T.; Toyokawa, H.; Ohgaki, H. Nondestructive detection of heavily shielded materials by using nuclear resonance fluorescence with a laser-compton scattering γ-ray source. *Appl. Phys. Express* **2009**, *2*, 036502. [CrossRef]

106. Bertozzi, W.; Korbly, S.E.; Ledoux, R.J.; Park, W. Nuclear resonance fluorescence and effective Z determination applied to detection and imaging of special nuclear material, explosives, toxic substances and contraband. *Nucl. Instrum. Methods Phys. Res. Sect. B Beam Interact. Mater. At.* **2007**, *261*, 331–336. [CrossRef]

107. Ferri, J.; Corde, S.; Döpp, A.; Lifschitz, A.; Doche, A.; Thaury, C.; Phuoc, K.T.; Mahieu, B.; Andriyash, I.; Malka, V.; et al. High-brilliance betatron γ-ray source powered by laser-accelerated electrons. *Phys. Rev. Lett.* **2018**, *120*, 254802. [CrossRef]

108. Geddes, C.G.; Rykovanov, S.; Matlis, N.H.; Steinke, S.; Vay, J.L.; Esarey, E.H.; Ludewigt, B.; Nakamura, K.; Quiter, B.J.; Schroeder, C.B.; et al. Compact quasi-monoenergetic photon sources from laser-plasma accelerators for nuclear detection and characterization. *Nucl. Instrum. Methods Phys. Res. Sect. B Beam Interact. Mater. At.* **2015**, *350*, 116–121. [CrossRef]

109. Banerjee, S.; Chen, S.; Powers, N.; Haden, D.; Liu, C.; Golovin, G.; Zhang, J.; Zhao, B.; Clarke, S.; Pozzi, S.; et al. Compact source of narrowband and tunable X-rays for radiography. *Nucl. Instrum. Methods Phys. Res. Sect. B Beam Interact. Mater. At.* **2015**, *350*, 106–111. [CrossRef]

110. Stöhr, J.; Wu, Y.; Hermsmeier, B.; Samant, M.; Harp, G.; Koranda, S.; Dunham, D.; Tonner, B. Element-specific magnetic microscopy with circularly polarized X-rays. *Science* **1993**, *259*, 658–661. [CrossRef]

111. Suzuki, M.; Yumoto, H.; Koyama, T.; Yamazaki, H.; Takeuchi, T.; Kawamura, N.; Mizumaki, M.; Osawa, H.; Kondo, Y.; Ariake, J.; et al. Magnetic microscopy using a circularly polarized hard-X-ray nanoprobe at SPring-8. *Synchrotron Radiat. News* **2020**, *33*, 4–11. [CrossRef]

112. Jourdain, N.; Chaulagain, U.; Havlík, M.; Kramer, D.; Kumar, D.; Majerová, I.; Tikhonchuk, V.; Korn, G.; Weber, S. The L4n laser beamline of the P3-installation: Towards high-repetition rate high-energy density physics at ELI-Beamlines. *Matter Radiat. Extrem.* **2021**, *6*, 015401. [CrossRef]

113. Edwards, J.; Rose, S. Ionization time scales in hot dense plasma. *J. Phys. B At. Mol. Opt. Phys.* **1993**, *26*, L523. [CrossRef]

114. Vinko, S.; Ciricosta, O.; Cho, B.; Engelhorn, K.; Chung, H.K.; Brown, C.; Burian, T.; Chalupský, J.; Falcone, R.; Graves, C.; et al. Creation and diagnosis of a solid-density plasma with an X-ray free-electron laser. *Nature* **2012**, *482*, 59–62. [CrossRef]

115. Weber, S.; Bechet, S.; Borneis, S.; Brabec, L.; Bučka, M.; Chacon-Golcher, E.; Ciappina, M.; DeMarco, M.; Fajstavr, A.; Falk, K.; et al. P3: An installation for high-energy density plasma physics and ultra-high intensity laser–matter interaction at ELI-Beamlines. *Matter Radiat. Extrem.* **2017**, *2*, 149–176. [CrossRef]